An integrated quantum-classical protocol for the realistic description of solvated multinuclear mixed-valence transition metal complexes and their solvatochromic properties

Giacomo Prampolini,[a,*] Amity Andersen,[b] Benjamin I. Poulter,[c] Munira Khalil,[c] Niranjan Govind,[c,d] Elisa Biasin[d,*] and Mariachiara Pastore[e,*]

[a]*Istituto di Chimica dei Composti OrganoMetallici* (ICCOM-CNR),
Area della Ricerca, via G. Moruzzi 1, I-56124 Pisa, Italy
[b]*Environmental Molecular Sciences Laboratory, Pacific Northwest National Laboratory*
Richland, WA, USA
[c]*Department of Chemistry, University of Washington*
Seattle, WA 98195, USA
[d]*Physical and Computational Sciences Directorate, Pacific Northwest National Laboratory*
Richland, WA 99352, USA
[e]*Laboratoire de Physique et Chimie Théoriques (LPCT), CNRS & Université de Lorraine*
54000 Nancy, France

November 28, 2023

*corresponding author: giacomo.prampolini@pi.iccom.cnr.it, elisa.biasin@pnnl.gov, mariachiara.pastore@univ-lorraine.fr

Abstract

Linear cyanide-bridged polymetallic complexes, which undergo photoinduced metal-to-metal charge transfer (MMCT), represent prototypical systems for studying long-range electron-transfer reactions and understanding the role played by specific solute–solvent interactions in modulating the excited state dynamics. To tackle this problem, while achieving a statistically meaningful description of the solvent and of its relaxation, one needs a computational approach capable of handling large polynuclear transition metal complexes, both in their ground and excited states, as well as the ability to follow their dynamics in several environments up to nanosecond timescales. Here, we present a mixed quantum classical approach, which combines large-scale molecular dynamics (MD) simulations, based on an accurate quantum mechanically derived force field (QMD-FF) and self-consistent QMD polarized point charges, with IR and UV-Vis spectral calculations to model the solvation dynamics and optical properties of a cyano-bridged trinuclear mixed valence compound (trans-$[(NC)_5Fe^{III}(\mu\text{-}CN)Ru^{II}(\text{pyridine})_4(\mu\text{-}NC)Fe^{III}(CN)_5]^{4-}$). We demonstrate the reliability of the QMD-FF/MD approach in sampling the solute conformational space and capturing the local solute-solvent interactions by comparing the results with higher-level quantum mechanics/molecular mechanics (QM/MM) MD reference data. The IR spectra calculated along the classical MD trajectories in different solvents correctly predict the red-shift of the CN stretching band in the aprotic medium (acetonitrile) and the subtle differences measured in water and methanol, respectively. By explicitly including the solvent molecules around the cyanide ligands and calculating the thermal averaged absorption spectra using time-dependent density functional theory (TDDFT) calculations within the Tamm-Dancoff approximation (TDA), the experimental solvatochromic shift is quantitatively reproduced going from water to methanol, while it is overestimated for acetonitrile. This discrepancy can likely be traced back to the lack of important dispersion interactions between the solvent cyano groups and the pyridine substituents in our micro solvation model. The proposed protocol is applied to the ground state in water, methanol, and acetonitrile and can be flexibly generalized to study excited state non-equilibrium solvation dynamics.

1 Introduction

As electron transfer (ET) reactions are central in a variety of biological and physicochemical processes, intensive research efforts have been devoted to understand and modulate the structural, electronic and environmental parameters governing mechanistic pathways.[1–3] In this context, polymetallic supramolecular structures, giving rise to metal-to-metal charge transfer (MMCT) are particularly interesting because of the variety offered by the possibility of modifying the coordination number, ligands and redox properties of the metallic centers. In particular, ambidentate cyanide ligands have been largely exploited to build polynuclear architectures, with moderate to strong metal-metal electronic coupling and appealing magnetic, photophysical, and electronic properties exploitable for different applications.[4–21] Moreover, linear cyanide-bridged assemblies have served as prototypical architectures for studying long range ET reactions. In these systems, excitation into the MMCT band initiates the transfer of an electron from one metal center to the other, and internal conversion from the excited state leads to a back electron-transfer (BET) reaction. Within this family, one of the most experimentally-characterized complex is $[(NC)_5[Fe]^{II}CN[Ru]^{III}([NH]_3)_5]^-$ (FeRu),[22–27] which upon photoexcitation undergoes BET with timescales ranging from tens to hundreds of femtoseconds depending on the employed solvent.[28]

A fundamental understanding of the role played by specific solute–solvent interactions in the photoinduced dynamics of FeRu and, more in general, of transition metal complexes (TMCs) with cyanide ligands[29–34] is a crucial question which joint experimental and computational investigations have been trying to answer.[27,35–37] The strong solvatochromic shifts of the CT bands in these systems is due to specific hydrogen bonding interactions between the cyanide ligands and the solvent molecules, with a strength proportional to the solvent acceptor number and the number of cyanide ligands.[38] Very recently, some of us reported an investigation of the ultrafast photoinduced dynamics of FeRu in water with femtosecond X-ray scattering and emission spectroscopy measurements. By combining these experiments with non-equilibrium molecular dynamics simulations, we showed that coherent translational motion of the water molecules hydrogen bonded to FeRu is coupled to the photoinduced MMCT and subsequent

ultrafast (62 fs) BET.[27] Clearly, from a theoretical and computational point of view, atomistic insights onto the solvent relaxation dynamics and their impact on the energetics and dynamics of charge transfer states can only be obtained by explicitly including the solvent molecules into the system and taking into account finite temperature effects.[27,35,39–45] Although nowadays, very efficient parallel implementations and machine learning (ML) techniques,[46–48] coupled to the increase of computational power, make it possible to run *ab initio* molecular dynamics (MD) simulations of rather complex systems.,[49–58] the necessity of treating very large systems (with thousands of solvent molecules to reliably account for the outer solvation shells) and reaching longer timescales (hundreds of picoseconds up to nanoseconds) often hinders the use of first-principles MD methodologies. Hybrid Molecular Mechanics (MM) and Quantum Mechanics (QM) schemes (QM/MM), which describe the solute at the QM level and the solvent by means of classical mechanics,[59–66] represent a valuable approach to treat large-sized systems, up to timescales on the order of picoseconds. On the one hand, ML approaches, trained on the potential-energy surface (PES) of QM subsystems, may now enable larger scale QM(ML)/MM simulations.[67–69] On the other hand, when dealing with large systems, targeting longer simulation timescales (nanosecond to microsecond) and/or reliably accounting for several embedding environments requires turning to classical techniques such as MD or Monte Carlo (MC).[70,71] In this framework, very accurate intramolecular and intermolecular force fields (FFs) and an adequate configurational sampling are crucial for the reliability of results extracted from classical MD simulations.[70–75]

The general approach in classical MD simulations is assuming FF parameters as general and transferable between different systems belonging to a similar family of compounds.[76–78] While this approach works rather well for biological systems,[79] and a variety of widely employed state-of-the-art FFs are implemented in commercial and open source packages,[80–85] practically no accurate transferable FF parameters, capable of describing the metal-ligand interaction and the coordination geometry, exist,[86,87] as well as no general-purpose parameters are available for molecules in their electronic excited states.[88] Alternatively, one can abandon the idea of generality and transferability and adopt a system-tailored approach to develop a very accurate FF for a specific molecule in a given electronic state. In this framework, a route to achieving

such specificity is to exploit the accuracy of QM calculations, deriving the FF parameters from a higher-level QM reference.[74] Since the first attempts[89–92] to provide a robust and automated procedure to provide such quantum mechanically derived force fields (QMD-FF),[90] the research topic has flourished,[75,93–107] as QMD-FFs can be applied in most cases where transferability fails, and experimental training data sets are lacking or totally missing.[74,75] For instance, mixed quantum classical strategies based on QMD-FFs have been successfully integrated in multi-level protocols for computational spectroscopy, exploiting the possibility of retrieving the required information for the parameterization of FFs suitable for excited states from the reference QM data.[43,100,105,108–111] Yet, among the plethora of proposed parameterization strategies, only a few of them seem able to handle the presence of metals coordinated to organic ligands, and automated QMD-FF parameterization procedures are mostly dedicated to metal organic frameworks (MOFs) and focus on the fine tuning of the intramolecular interactions.[93,96,97,99] The structure and dynamics of specific monovalent TMCs, for which general purpose parameters were incomplete or unreliable, has been investigated through a QMD-FF strategy also by some of us,[42–44,112] achieving promising results in the description of the solvent dependent vibrational features,[112] internal structure[44] and, most recently, optical behavior.[42,43]

In the present paper we expand on this by extending the intra-molecular parameterization procedure to a polymetallic complex, and additionally, we propose a general procedure to refine the intermolecular term of the FF, based on a QM description consistent with the one employed to parameterize the valence term. The target compound to which our QMD-FF strategy will be applied is trans-$[(NC)_5Fe^{III}(\mu\text{-}CN)Ru^{II}(\text{pyridine})_4(\mu\text{-}NC)Fe^{III}(CN)_5]^{4-}$ shown in Figure 1.a and hereafter referred as **FeRuFe**. This is one of the few structurally characterized linear trimetallic compounds containing terminal cyanides,[113] and represents a significant increase in complexity with respect to the FeRu molecule previously investigated by some of us.[27] Here we focus on the solvation dynamics, infrared (IR) and Uv-Vis absorption spectra of **FeRuFe** in three different solvents, namely water, methanol (MeOH) and acetonitrile (MeCN), demonstrating the reliability of our QMD-FF/MD approach in sampling the solute conformational space and capturing the local solute-solvent interactions when compared to higher-level QM/MM MD reference data. The present methodology, applied here to the ground state properties, can be ef-

ficiently generalized to excited states, paving the way towards reliable atomistic simulations and a fundamental understanding of solute-solvent ultrafast relaxation dynamics upon photoinduced MMCT excitation and subsequent BET.

2 Methods

2.1 Computational protocols

General scheme

Our proposed multi-level computational protocol integrates QM calculations, which can accurately capture **FeRuFe** structural and electronic features, and classical techniques, to reliably introduce solvent and thermal effects. Hence, the **FeRuFe** complex, shown in Figure 1, is first investigated at the QM level by exploring selected regions of its potential energy surface and the response of its electronic density to the presence of specific solvents. The resulting information is encoded in a **FeRuFe** specific QMD-FF, parameterized to best reproduce the computed QM descriptors and suitable for classical MD simulations. MD runs are thereafter carried out for the solvated **FeRuFe** complex, taking into account different solvents and monitoring the solute behavior for several ns, hence ensuring a reliable statistics. The resulting trajectories are eventually used to analyze the different solvation structures among the considered solvents, as well as statistical ensembles to compute thermally averaged IR and UV-vis spectra.

QM calculations

The QM chemical descriptors required for **FeRuFe**'s ground state FF parameterization were computed at the density functional theory (DFT) level, using the PBE0 functional.[114,115] Specifically, these descriptors are the **FeRuFe**'s optimized geometry (g_0), its Hessian matrix ($\hat{\mathbf{H}}^{QM}_{|g_0}$) and the relaxed torsional energy scans $\Delta E^{QM}_{intra}(\delta_{CN})$ and $\Delta E^{QM}_{intra}(\delta_{pyr})$ of the flexible dihedrals, where the δ_{CN} dihedral govern the rotation of the equatorial cyano groups (Cz_2Nz_2, see Figure 1 for definition) around the $\hat{C}_4$ axis, while the δ_{pyr} dihedral drives the rotation of the pyridyl substituents around the Ru-N bond. The triple-ζ polarized 6-311G(d,p) basis set[116,117] was employed for all atoms except the two Fe atoms and Ru atom, which were represented with the Stuttgart RSC 1997 ECP.[118,119] The choice of the PBE0 functional has been recently bench-

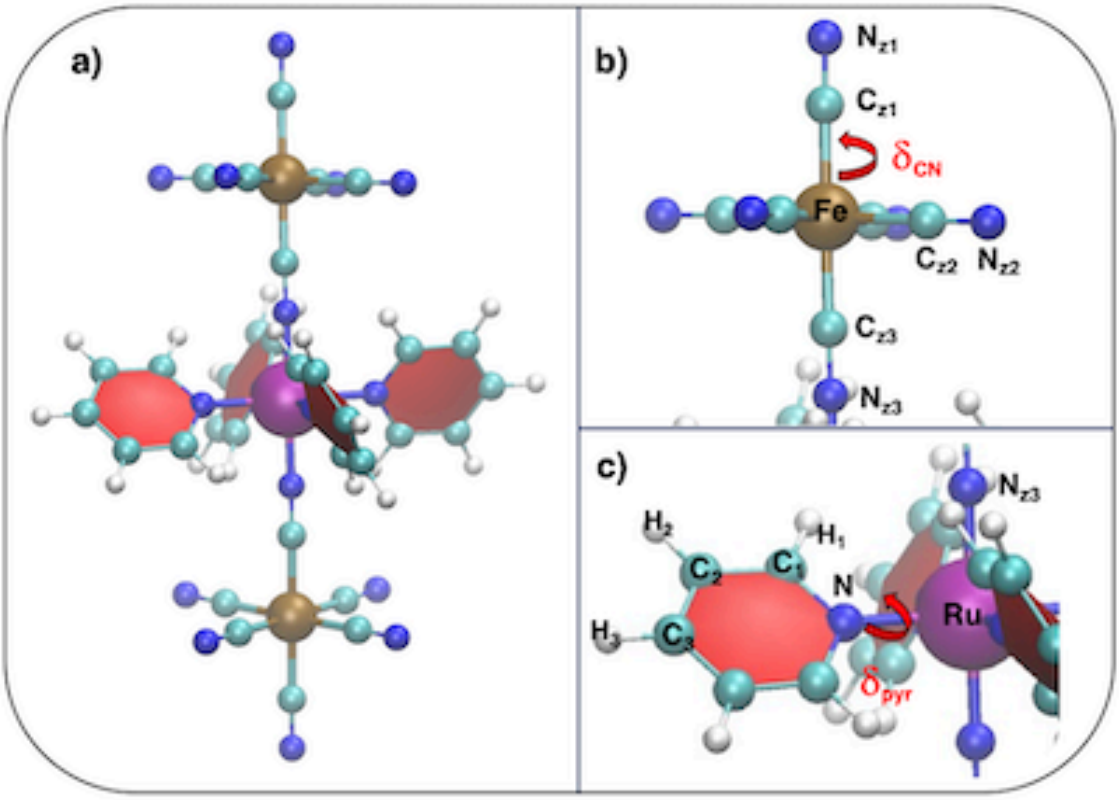

Figure 1: Structure and labeling of $[(NC)_5Fe^{III}(\mu\text{-}CN)Ru^{II}(pyridine)_4(\mu\text{-}NC)Fe^{III}(CN)_5]^{4-}$ (**FeRuFe**). a) QM optimized structure of **FeRuFe**; b,c) QMD-FF specific atom types and flexible dihedrals (see also Figures S1 and S2 in the Supporting Information). We indicate as z1, z2, and z3 the terminal, equatorial and bridging cyanide ligands respectively.

marked by some of us of the FeRu complex.[26,27,120] Since in that case the baseline characteristics of the metal dimer (including charge transfer) were captured with sufficient accuracy compared with experiment, considering the similarity with the present complex, we chose to maintain PBE0 also for **FeRuFe**, so that we can eventually compare the photophysics between the dimer and trimer systems. In consideration of the high charge of the investigated complex, the calculations of the aforementioned descriptors were performed accounting for the solvent through the polarizable continuum method (PCM).[121]

Vertical excitation energies (VE), either computed at the optimized g_0 geometry or over the snapshots extracted from the MD trajectories, were consistently performed with the PBE0 functional, but, to minimize the computational burden, with a smaller basis set (6-31G*) and

adopting the Tamm–Dancoff approximation (TDA).[122] As shown in Figure S10 in the Supporting Information, the chosen PBE0/6-31G* level of theory was successfully benchmarked against both the larger basis set and a different functional. These DFT and TDA calculations were carried out with the GAUSSIAN16 package.[123]

QM/MM calculations

An initial optimized conformation of the **FeRuFe** complex was solvated in a $62 \times 62 \times 62$ Å^3 box of 7919 water molecules and four sodium cations (Na^+), using the preparation tools and a pre-prepared equilibrated bulk water template available in the NWChem computational chemistry software package.[124,125] In the subsequent QM/MM simulations, **FeRuFe** was assigned to the QM region, while all water molecules and cations were assigned to the MM region. Within the former region, the same level of theory was employed as in the previously described QM calculations (PBE0) for consistency, again using the 6-311G** basis set for the light atoms, H, C, and N,[116,117] and the Stuttgart scalar relativistic basis set and effective core potentials (ECP) for Fe and Ru.[118,119] At the QM/MM interface, the van der Waals parameters for the C, N, and H atoms of the **FeRuFe** complex were obtained from the general AMBER FF (GAFF) set, [126] whereas the Fe and Ru atoms of the complex were described through the CLAYFF FF of Cygan et al.,[127] employing AMBER 1-4 and Lorentz-Berthelot mixing rules for the non-bonded interactions. Finally, in the MM region, water molecules were described through the extended single point charge water model (SPC/E) of Berendsen and co-workers,[128] while for Na^+ the classical FF of Joung and Cheatham[129] was employed. The system was thereafter optimized with the NWChem QM/MM module, applying the SHAKE algorithm[130] only to the water molecules, to constrain the bond lengths and angle, as prescribed by the SPC/E potential. The cut-off for the coulombic interactions was set to 12 Å. The QM/MM interaction zone surrounding the complex was set to 20 Å. Geometry optimization was performed cyclically (for a maximum of 5 times until convergence), each cycle consisting in a maximum of 10 Broyden-Fletcher-Goldfarb-Shanno (BFGS) iterations in the QM region, followed by a maximum of 3000 steepest-descent (SD) iterations in the MM zone. Following optimization, QM/MM dynamics were performed. Initially, the complex was held fixed and the water solvent was allowed to equilibrate over 10 ps with a time step of 2 fs and using the Berendsen's thermostat[131] for

NVT simulations at 298.15 K. Subsequently, the complex was allowed to equilibrate with the solvent for 1 ps and a time step of 0.25 fs. Following 1 ps, QM/MM dynamics of the entire system was performed for another 20 ps.

QMD-FF parameterization

A specific QMD-FF was assembled for **FeRuFe** exploiting the classical partition of the total FF energy in an intramolecular term, governing the shape and flexibility of the complex, and an intermolecular term, which describes its interactions with the surrounding solvent:

$$E_{tot}^{QMD-FF} = E_{intra}^{QMD-FF} + E_{inter}^{QMD-FF} \tag{1}$$

The parameterization of the FF's intramolecular term has been carried out with the JOYCE software,[132] which allows one to derive a E_{intra}^{QMD-FF} term based on the QM data specifically computed for the **FeRuFe** monomer, as described in the previous section. According to the standard JOYCE protocol,[90,133,134] the best QMD-FF parameters are thus retrieved by minimizing the objective function

$$I = \frac{1}{N_{geom}} \sum_{g}^{N_{geom}} W_g \left[\Delta E_{intra}^{QM} - E_{intra}^{QMD-FF} \right]_g^2 + \sum_{K \leq L}^{3N-6} \frac{2W''_{KL}}{(3N-6)(3N-5)} \left[H_{KL}^{QM} - \left(\frac{\partial^2 E_{intra}^{QMD-FF}}{\partial Q_K \partial Q_L} \right) \right]_{g=0}^2 \tag{2}$$

where the first sum runs over the N_{geoms} **FeRuFe**'s geometries considered in the δ_{CN} and δ_{pyr} dihedral scans, and the second (double) sum runs over the $3N$-6 QM normal modes (N being the number of **FeRuFe** atoms) obtained at $g = 0$. The W_g and W''_{KL} terms are user-defined weights: the normalized diagonal elements of the weight matrix $\mathbf{W}''$ are set as in similar previous applications,[42,43,112] at twice the value of those corresponding to the off diagonal terms, while weights W_g have the same value for all the considered geometries. Further details concerning JOYCE parameterization are reported in Section A of the Supporting Information or can be found in the original papers.[90,133,134]

E_{inter}^{QMD-FF}, the intermolecular FF term appearing in equation (1), was computed through the standard pairwise sum of Lennard Jones (LJ) and Coulomb (charge-charge) interactions:

$$u_{ij}^{inter} = 4\varepsilon_{ij}^{inter} \left[\left(\frac{\sigma_{ij}^{inter}}{r_{ij}} \right)^{12} - \left(\frac{\sigma_{ij}^{inter}}{r_{ij}} \right)^{6} \right] + \frac{q_i q_j}{r_{ij}} \tag{3}$$

where ε_{ij}^{inter} and σ_{ij}^{inter} are the LJ parameters and q_i and q_j the point charges. Following previous QMD-FF parameterization carried out by some of us for simpler, monovalent TMCs,[42–44,112] the LJ parameters for **FeRuFe**ˆ were taken from literature databases (either OPLS,[77,78] for pyridiyl and cyano groups, or previous FF parameterization,[135,136] of TMCs, for the metal atoms) and combined, through the OPLS mixing rules,[81] with the solvent parameters (either TIP3P[137] for water or OPLS[77,78] for methanol and acetonitrile). In keeping with the QMD-FF intramolecular term, the Coulomb interaction term of u_{ij}^{inter} in equation (3) was also derived from QM data and tailored to mimic the **FeRuFe** interaction specifically for each solvent. To this end, an automated iterative procedure to retrieve QM derived polarized point charges (QMD-*p*PC) is proposed, summarized in Figure 2 and detailed in the following. For each considered

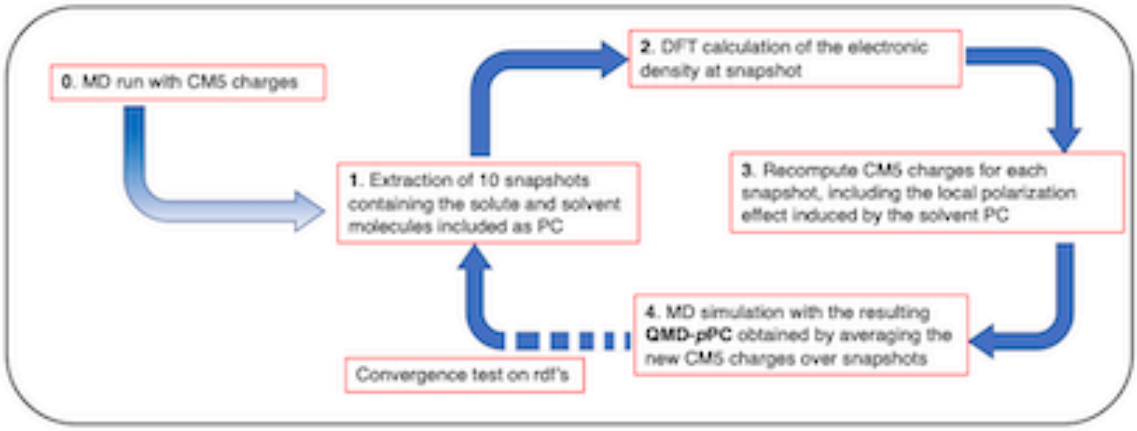

Figure 2: Scheme of the iterative parameterization procedure devised to obtain Quantum Mechanically Derived polarized Point Charges (QMD-*p*PC).

solvent, point charges are first derived through the CM5 scheme[138] from the QM electronic density, specifically computed for **FeRuFe** at the PBE0 level, taking the solvent into account at an implicit level, through the PCM scheme.[121] The resulting charges are then employed in a preliminary MD simulation, carried out on a system composed of one **FeRuFe** complex and more than 3000 solvent molecules (see next section for details). A set of ten uncorrelated snapshots are extracted from the equilibrated MD trajectories, containing the coordinates of the **FeRuFe** complex and all solvent molecules within a 14 Å radius shell. A new QM calculation

is then carried for each extracted snapshot, again obtaining atomic charges of the **FeRuFe** complex through the CM5 scheme,[138] but explicitly accounting for the solvent, by including in the calculation all solvent atoms as point charges, using the same values in the MD runs (i.e. TIP3P for water or OPLS for the other two solvents). A new set of charges for **FeRuFe** is then obtained by averaging, for each atom, the values obtained over the 10 sampled snapshots. This procedure is thereafter iteratively repeated until convergence, which was assessed by comparing the solvent structure around the most interacting **FeRuFe** complex atoms, revealed by specific radial correlation functions computed along the MD trajectories at each parameterization step. We call the resulting charges *polarized* since the atoms of the complex which mostly interact with the surrounding solvent are expected, with respect to an implicit model, to be more specifically polarized by the average network of embedding charges.

Molecular Dynamics

MD runs were carried on systems composed by one **FeRuFe** complex surrounded by large numbers of solvent molecules, namely 7960, 3349 and 3343 for water, methanol or acetonitrile, respectively. To neutralize the high negative charge of the TMC, four Na^+ cations were also included in the simulation boxes. After a first 500 ps preliminary equilibration at 298 K in the NVT ensemble, longer equilibration runs (2 ns) were carried out in at constant temperature (298 K) and pressure (1 atm) for each solvent. Finally, MD production runs of 5 ns were launched again in the NPT ensemble, saving the trajectories every 1 ps. In all cases, temperature and pressure were kept constant through the v-rescale[139] and the Parrinello-Rahman[140] algorithms, respectively. In all runs, long range electrostatic was accounted for with particle mesh Ewald (PME), while a cut-off distance of 12 Å was employed for short-range interactions, applying the standard correction for energy and virial[70] applied to LJ potentials. During all simulations, no constraints were applied on the bond lengths and the time step was set to 0.1 fs, which allowed for a correct energy conservation on the NVE runs eventually carried out the three solvated systems to compute the dipole correlation functions (see next section). All MD runs were carried out with the GROMACS package,[81]

IR and UV spectra calculation

The IR vibrational frequencies were recovered for each solvent over 1 ns NVE MD runs, from

the dipole moment correlation function according to[141]

$$I(\nu) \propto Q(\nu)\nu \int_0^\infty e^{i2\pi\nu t} \langle \bar{\mu}(t+t_0)\bar{\mu}(t) \rangle \, dt \tag{4}$$

where $\bar{\mu}(t)$ is the dipole moment computed along the MD runs at classical level as

$$\bar{\mu}_i(t) = \sum_{\alpha=1}^{N} q_\alpha r^*_{i\alpha}(t) \tag{5}$$

where q_α and $r^*_{i\alpha}(t)$ are respectively the QMD-pPC charge on atom α of the **FeRuFe** complex and its displacement with respect to the center of mass of the complex, N is being the total number of TMC atoms. The function $Q(\nu)$ in equation 4 is a QM correction,[142] given by

$$Q(\nu) = \frac{\beta h\nu}{1 - e^{-\beta h\nu}} \tag{6}$$

with $\beta = 1/k_B T$, where is the k_B Boltzmann constant and T simulation temperature.

A preliminary description of the UV spectra in the different solvents was first achieved by applying a procedure solely based on a single optimized conformer of the **FeRuFe** complex, taking the solvent into account as a continuum through the PCM scheme.[121] Such procedure will be hereafter referred as 'static', because the spectral signal is obtained by applying a phenomenological Gaussian broadening to the computed vertical transition energy without explicitly considering neither solutes's not solvent's dynamics. Conversely, thermally averaged UV absorption spectra were obtained according to a mixed quantum-classical scheme based on a classical ensemble average of vertical energies (CEA-VE), recently employed to reproduce steady-state and transient UV spectra of a Ru heteroplectic TMC.[42,43] Specifically, dynamical and explicit solvation effects were included in the **FeRuFe** electronic absorption spectra by averaging the TDA vertical excitation energies computed along 100 uncorrelated snapshots, extracted from the MD runs carried out in ambient conditions with the QMD-FF. The final absorption spectra were eventually obtained by a Gaussian convolution with 0.1 eV half-width-half-maximum (HWHM), considering the 100 lowest transitions for each frame. Finally, to gain a deeper insight onto the different contributions (e.g. electrostatic, polarization, etc.) to the solute-solvent interactions determining the spectral shape, two different models were employed to account for the explicit solvation at different levels of accuracy. In model **I**, for each

extracted snapshot, beside the coordinates of the **FeRuFe** complex, which are treated at the QM level, all solvent molecules lying within a r_{cut}^{PC} radius from the Ru atom are included as PC (with the same values employed in MD simulations, as in the QMD-*p*PC procedure), thus accounting for the local and specific polarization effects induced by the solvent charges on the TMC solute molecule. Conversely, in model **II**, all solvent molecules found within a specific radius r_{cut}^{QM} from the most interacting **FeRuFe** atoms (Cz and Nz, see Figure 1.b), as revealed by the solvent structure analysis along the MD runs) are included in the calculations at QM level, whereas the rest of the solvent is accounted for at the PCM level. It is worth noting that within this scheme, the local mutual polarization effects between the solvent and the solute are also introduced in the prediction of the spectral shape.

2.2 Experimental setup

Sample preparation

Na and $P(Ph)_4$ salts of trans-$[py_4Ru^{II}\{NC\text{-}Fe^{III}(CN)_5\}_2]^{4-}$ were synthesized following previously established literature procedures.[113,143] In summary, trans-$[Ru(py)_4Cl_2]$ and $K_3[Fe(CN)_6]$ (in excess) were dissolved in a 4:1 mixture of water and methanol. This solution was then refluxed under nitrogen for four hours. Excess methanol was then added to precipitate unreacted $K_3[Fe(CN)_6]$ and the solution was filtered. The filtrate was treated with excess $P(Ph)_4Cl$ to create a green slurry. This was filtered an additional time to collect a green solid. This solid was then dissolved in minimal amounts of methanol and purified with exclusion chromatography using a Sephadex LH-20 packed column eluted with methanol. The dark green fraction from the column was collected and further purified by recrystallization from methanol/diethyl ether. To prepare the sodium salts, the $P(Ph)_4$ salts were dissolved in acetonitrile and treated with excess $NaClO_4$ which caused immediate precipitation. This solid was then collected by filtration, dissolved in water, filtered again, and the resulting filtrate was dried with a rotary evaporator yielding pure Na_4FeRuFe salts. Pyridine and Acetonitrile were purchased from Fisher Chemical; all other precursors and solvents were purchased from Sigma-Aldrich and used without further purification. Solvents used during the synthesis and for spectroscopic measurements were of HPLC grade 99.9% purity.

Spectroscopic measurements

Solutions for spectroscopy were prepared by dissolving $(P(Ph)_4)_4FeRuFe$ in methanol and acetonitrile and $Na_4FeRuFe$ in water and heavy water (D_2O) to yield 25mM solutions. IR spectra were recorded on a Jasco FT/IR 4700 spectrometer using the above solutions and a sample cell with a 50 μm pathlength. UV-vis-NIR spectra were recorded on a Varian Cary 5000 UV-vis-NIR spectrophotomer using the same solutions and sample cell. All spectra were processed by subtracting solvent only spectra from the spectra of the 25mM solutions. Note that the IR spectra of D_2O is shown instead of water, since the spectra were nominally identical but solvent subtraction was easier for D_2O.

3 Results

3.1 QMD-FF validation

The QMD-FF intramolecular term was parameterized through the JOYCE procedure,[90,134] based on the QM descriptors specifically computed for **FeRuFe** at the DFT level as reported in the previous section. The parameterization was carried out on a set of 620 redundant internal coordinates, fitting 55 independent parameters with a final standard deviation of 1.05 kJ/mol. All final intramolecular parameters are given in Section C of the Supporting Information, while further details concerning the applied JOYCE procedure can be found in Section A.

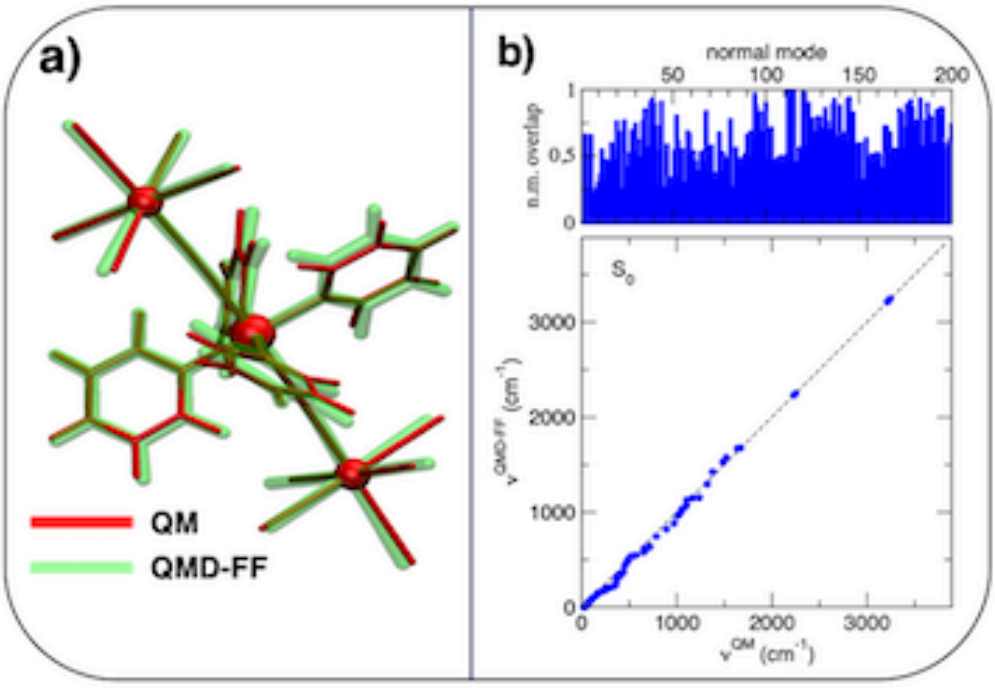

Figure 3: Summary of QMD-FF intramolecular parameterization. a) overlap of QM (DFT/PBE0, red sticks and spheres) and QMD-FF (green sticks and spheres) optimized structures; b) comparison between QM and QMD-FF vibrational frequencies (bottom) and normal mode (overlap, top).

The resulting intramolecular QMD-FF was validated by comparing selected features with

their QM counterparts, as summarized in Figure 3. First, the structure of the **FeRuFe** complex, optimized either at QM level or with the QMD-FF, are compared visually (Figure 3.a) and through the root mean square deviation (RMSD) with respect to the reference DFT structure (see Table 1). Next, the vibrational frequencies, computed at the QM and QMD-FF levels, are correlated as shown in Figure 3.b. Both tests appear to support the quality of our QMD-FF to reliably mimic the equilibrium structure of the **FeRuFe** complex and the distortions which might be induced by small amplitude oscillations in a local harmonic approximation. In particular, the

	Bond lengths (Å)	Bending angles (deg)	Dihedrals (deg)
RMSD	0.001	0.943	6.0

Table 1: RMSD between QM and MM optimized geometries in terms of bond lengths, bending angles and dihedrals.

specificity of the adopted atom labeling (see panels b) and c) in Figure 1) allows for differentiating atom types which are usually not distinguished by general-purpose FFs. For instance, as reported in Table S2 in the Supporting Information, the QMD-FF is able to distinguish among the different metal-ligand equilibrium lengths and force constants which govern the octahedral structure around the metals (see Fe-C_{Z1}/Fe-C_{Z2}/Fe-C_{Z3} and Ru-N_{Z3}/Ru-N, for Fe and Ru, respectively). Similarly, tailoring QMD-FF parameters over the proper QM relaxed torsional profiles, allows to accurately reproduce also more subtle features induced by larger distortions, as the coupling between the dihedrals ruling the rotation of the pyridiyl substituents around the $\widehat{N-Ru-N}$ axis (see Section D and Figures S1 and S5 for further details). A further confirmation of the QMD-FF reliability in exploring the conformational space of the **FeRuFe** complex comes from the comparison of the distribution of selected internal coordinates, computed along the MD trajectories carried out with our FF or at QM/MM level, and shown in the left panels of Figure 4. In fact, apart from a slight overestimation of the average Fe-Ru distance, both the coordination sphere around the Fe atom and the carbon backbone of the aromatic rings agree well with the higher level reference data.

The QMD-FF accuracy in accounting for solute-solvent interactions was tested by resorting again to our QM/MM molecular dynamics simulations, comparing the resulting solvation

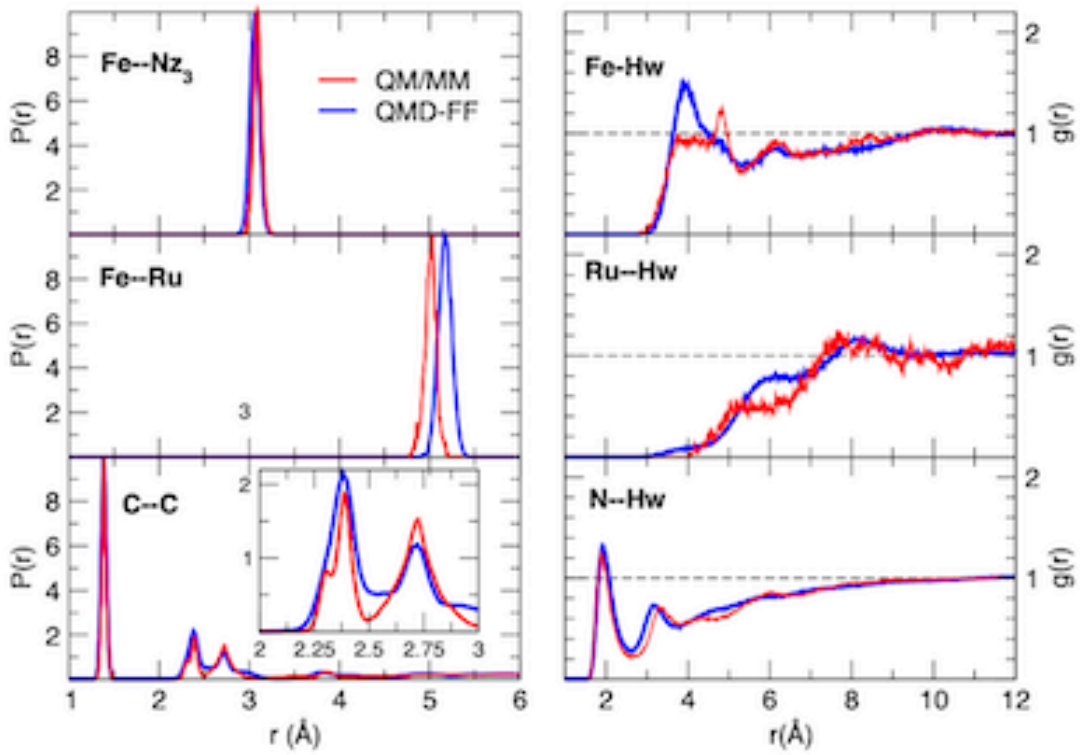

Figure 4: Validation of the QMD-FF (blue lines) for **FeRuFe** in water with respect to QM/MM molecular dynamics (red lines). Left panels: population distribution of relevant intra-molecular distances. Right panels: radial distribution functions between relevant **FeRuFe** atoms (Fe, Ru and all nitrogens) and the water proton (Hw).

structures with the one obtained through classical MD simulations carried out with our FF. Solute-solvent radial distribution functions, g(r), computed along the QMD-FF/MD trajectory between selected **FeRuFe** atoms and the water hydrogen (H_w), are shown in the right panels of Figure 4: the good overall agreement with the one obtained with the higher level technique confirms the capability of the classical approach to reliably mimic both the flexibility of the **FeRuFe** complex and its interaction with the surrounding environment. In particular, as also evidenced in Figure S6 in the Supporting Information, both the QM/MM and the classical MD simulations agree in indicating the N_{z1} and N_{z2} atoms as the most interacting **FeRuFe** sites. The radial distribution functions between $N_{z1/z2}$ and the water hydrogens (H_w) show peaks at short distances and with high intensities, hence suggesting the formation hydrogen bonds (HBs)

between the terminal and equatorial cyanide ligands and the surrounding solvent molecules.

Finally, it is worth noting that the QMD-FF parameterization protocol, adopted for **FeRuFe** in water, is rooted in the partition in intra- and intermolecular terms reported in equation (1), which can be exploited to obtain QMD-FFs designed for different embeddings in a straightforward way. In fact, the JOYCE accurate description of the flexibility of the **FeRuFe** complex can be exported to the new FF without any further calculations, whereas QMD-*p*PC can be recomputed for any specific solvent by applying the iterative protocol outlined in Figure 2. In turn, the possibility of employing accurate and system-specific QMD-FFs allows for atomistic insights into the effects of larger number of solvation shells and for longer simulation times compared with more computationally demanding QM/MM dynamics. Furthermore, as it will be shown in the following section, it also paves the way toward the simulation of different embedding environments, allowing for a balanced comparison of different solvation structures around the TMC.

3.2 Solvent effects on FeRuFe conformational dynamics

With the aim of investigating the different supramolecular networks settled by embeddings of varied polarity/proticity and their effect on the conformational dynamics of **FeRuFe**, the QMD-FF parameterization procedure adopted in water was extended as described in the previous sections to MeOH and MeCN. Figure 5 shows the distributions of selected **FeRuFe** dihedral angles achieved along the 5 ns production runs in the three different solvents at ambient conditions. Despite a direct evaluation of such conformational behavior is in this case inaccessible to experiment, the reliability of a QMD-FF description of flexible degrees of freedom was recently validated against single-molecule real measurements,[144,145] hence prompting us to confidently consider the simulated outcomes. As far as the stiff dihedral governing the symmetry around the Fe atom (ξ, see Figure S1) is concerned, the narrow overlapping peaks obtained in all cases indicate that solute-solvent interactions only negligibly perturb the octahedral structure of the ligands around the metal. The same results (not shown) have been obtained for ζ, which rules the disposition of the ligands around the Ru atom. On the contrary, the more flexible dihedrals describing the rotation of either the equatorial $C_{z2}N_{z2}$ ligands around the $\widehat{N_{z1}-Fe-N_{z3}}$ axis

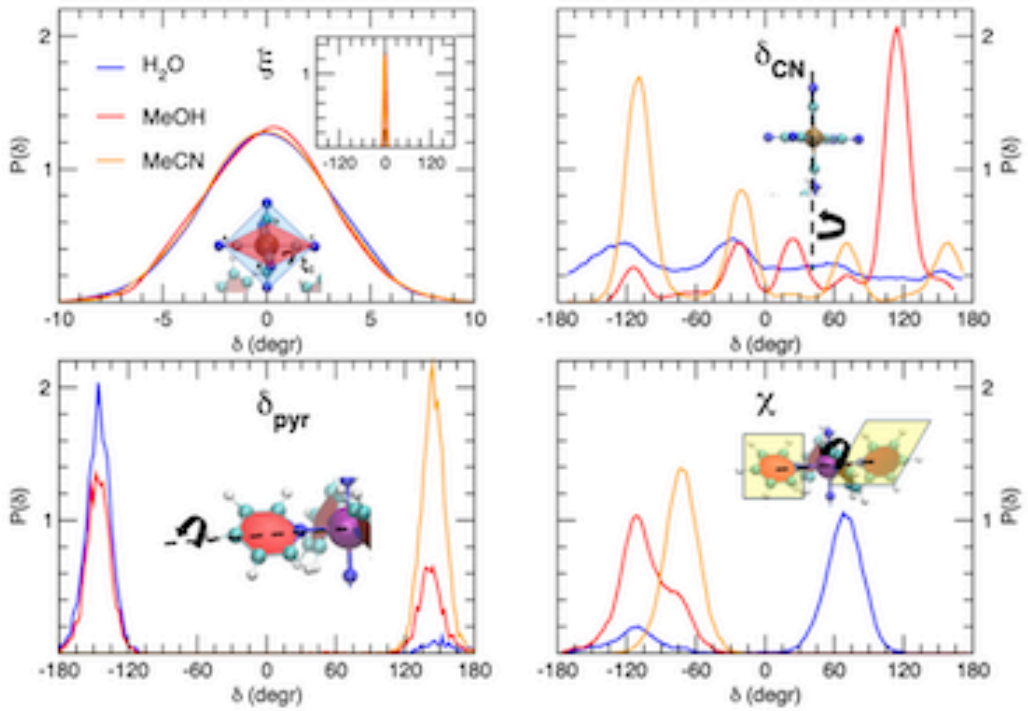

Figure 5: Selected dihedral distributions achieved in MD with different solvents, namely water (blue), methanol (red) and acetonitrile (orange). In the insets a pictorial definition of the considered dihedral is shown for clarity (see also Figure S1).

(δ_{CN}) or the pyridiyl groups around the Ru-N bonds (δ_{pyr}) show different behavior depending on the solvent. A similar behavior is registered also for χ, which measures the dihedral angle between the planes of two opposite pyridiyl rings. Although the non-symmetric peak distributions of the most flexible dihedrals suggest that 5 ns are not sufficient for a full exploration of the configurational space of solvated system, the different peak intensities registered in varied solvents for both δ_{pyr} and δ_{CN} clearly indicate for **FeRuFe** a solvent-dependent conformational dynamics. Interestingly, the above findings show that the δ_{CN} rotation is indeed greatly affected by the solvent nature, which appears to be able to significantly influence the conformational dynamics of the **FeRuFe** complex across the populated minima, again indicating that the stronger solute-solvent interactions are established with the polar $C_{z1}N_{z1}$ and $C_{z2}N_{z2}$ groups. Considering δ_{pyr}, a larger flexibility is observed for methanol with respect to the other two solvents, as

indicated by the population of two different minima in methanol. Notwithstanding the average octahedral symmetry is maintained in all cases and the distributions of most of the stiff coordinates show a negligible dependence on the surrounding solvent, finer effects take place on the internal modes more affected by the interaction with the solvent, as the Cz-Nz stretchings possibly directly involved in HBs with the surrounding water or MeOH molecules.

To ascertain this hypothesis, IR vibrational spectra were computed along the QMD-FF/MD trajectories for all solvents according to equation (4) and the results are plotted in the left panel of Figure 6. In the inset, the overall good agreement registered, along the whole explored frequency range, with the gas phase spectrum computed at pure QM level from the DFT Hessian matrix further confirms the quality of the QMD-FF. Yet, the spectra computed in different solvents show slight differences, which are enhanced when focusing on a narrower frequency range ($\sim$ 2120-2130 cm^{-1}), corresponding to the the C_z-N_z stretching modes computed at QM level in the gas phase C_z-N_z. The right panel of the same Figure shows FTIR spectra of **FeRuFe** in the three different solvents. The spectrum measured in water resemble the spectrum of the FeRu molecule in D_2O, where the peaks from lower to higher energies have been assigned to the stretching of the terminal, equatorial, and bridging cyanide ligands, respectively.[147] The comparison of the simulated IR peaks with the experimental signals appears to confirm computational predictions for the main peak position: the red-shift found for the aprotic solvent (MeCN) is also evident in the experiment, as well as the slight red shift found in water with respect to MeOH. The calculations also predict shoulders at higher wavenumbers, which contribute at the different spectral broadening also observed in the experiment. The underestimation of the spectral broadening may be traced back to the classical approximation employed for computing the dipole moment of **FeRuFe** and to the neglect of the quantum nature of the nuclear dynamics of **FeRuFe** and solvent interactions, whose inclusion would require the application of much more computationally expensive protocols,[109–111,148] which are beyond the scope of the present work.

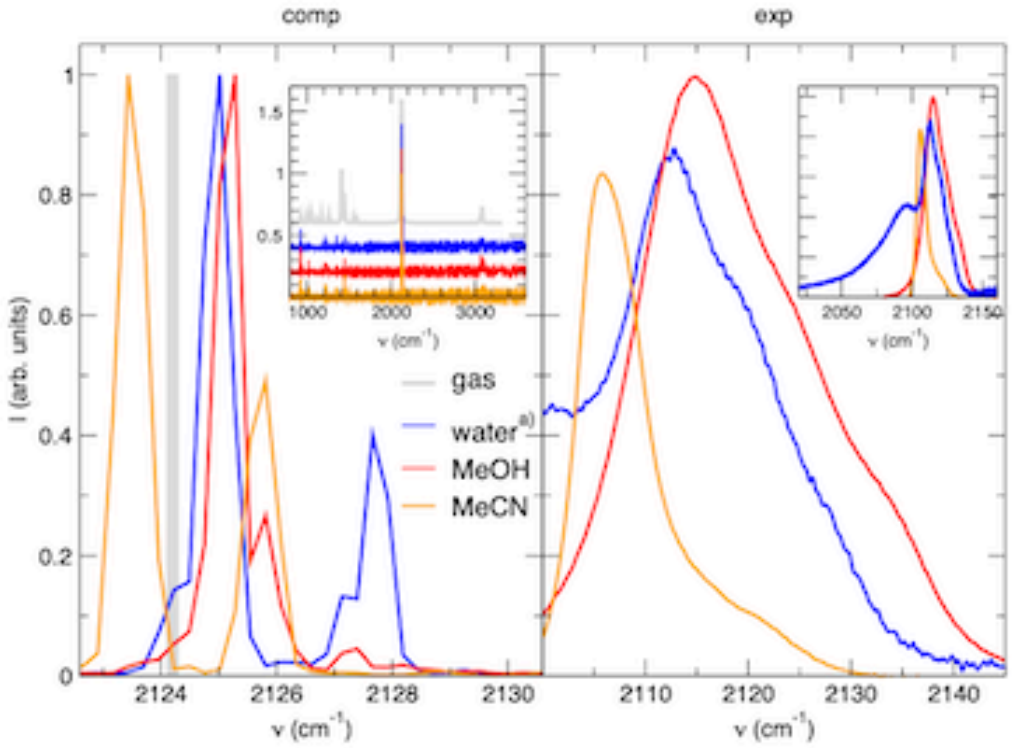

Figure 6: IR vibrational bands related to C_z-N_z stretching mode. Left: computed spectra for **FeRuFe** in gas phase (from the QM Hessian, gray line) and in the three solvents (water, methanol and acetonitrile), along the MD trajectories, according to equation 4. In the inset, the vibrational spectrum is displayed in the whole computed range. To better compare with experimental values, all frequency were scaled following Ref. [146]. Right: experimental spectrum in the $\sim$ 2100-2145 cm^{-1} region ([a)] registered in D_2O). In the inset, the same FTIR spectra are shown in a wider range.

3.3 FeRuFe solvation

The validated reliability of the QMD-FF description allows for confidently exploiting the wide range of length and time scales spanned by MD simulations to gain a deeper insight onto the varied solvation structures and their different effect on the electronic density of **FeRuFe**. For a qualitative comparison among the investigated solvents, spatial density functions (SDFs) were computed along the three equilibrated runs, and are displayed in Figure 7. Quite different solvation shells are already revealed by a first visual inspection. In water, solvent molecules are much more closely bonded and structured around the cyano ligands, whereas a more uniform density is settled around the aromatic substituents. Conversely, the less polar and aprotic sol-

vent (MeCN) shows less bounded solvent molecules around the cyano groups and an increased density in the region surrounding the pyridiyl ligands. MeOH solvation structure appears to be an intermediate case, where solvent molecules tend to settle at larger distances and more loosely bound with respect to water, as indicated by the wider density region.

The differences among the solvation shells evidenced in Figure 7 can be related to the different type and strength of the intermolecular interactions settled with the solvent, which can be distinguished in mainly arising from a pure Coulomb interaction (e.g. HBs) or connected to the dispersion forces established by the solvent with the π cloud of the aromatic ligands (Van Der Waals terms). Table 2 reports the total solute-solvent interaction energy, $U^{FeRuFe-solv}$, averaged along the MD runs, as well as the separate contribution of the Coulomb and LJ terms appearing in equation (3). The registered trends closely reflect the conclusions drawn with the SDF analysis, being water the most interacting solvent, while less favorable interaction energies are found for MeOH and, to a greater extent, for MeCN. Nonetheless, the origin of such interaction

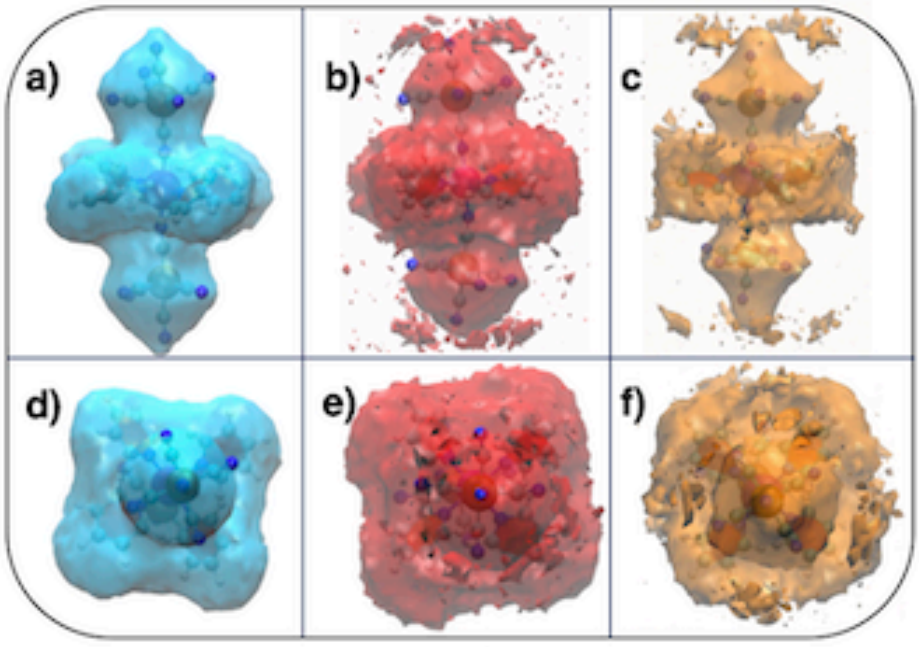

Figure 7: Side (top panels) and top (bottom panels) views of the SDFs of the Hw, Ho and Hc protons, achieved in MD carried out on **FeRuFe** in water (blue, a) and d) panels), methanol (red, b) and e) panels) and acetonitrile (orange, c) and f) panels).

is markedly different when considering the two protic solvent with respect to MeCN. In fact, in both water and MeOH, the largest contribution to $U^{FeRuFe-solv}$ comes from the Coulomb charge-charge interaction in equation (3), which is stronger in the former solvent, thanks to the higher number of HBs settled with the cyano ligands and reported in the last row of Table 2. In MeCN, on the contrary, the LJ terms play a much more relevant role, being the Van der Waals contribution more than half the Coulomb term.

3.4 Absorption spectra and solvatochromic shifts

The analysis of the solvent structure around the **FeRuFe** complex points to interactions of significantly varied strength and nature, which are expected to act differently on the electronic density of the TMC and, consequently, on its spectral properties. In particular, the local and specific interactions between the protic solvents and the cyano ligands are not expected to be well represented when adopting a continuum description for each considered embedding. For this reason, the information retrieved by the radial distribution functions is exploited to build two different models through which explicit solvent molecules can be reliably included in the calculation of the absorption spectrum. Figure 8 illustrates the two adopted models for the water solvent, whereas Figures S7 and S8 refer to MeOH and MeCN solvents, respectively. In model **I**, the solvent molecules are explicitly accounted for as point charges (PC), including molecules within r_{cut}^{PC} = 14 Å with respect the Ru atom, i.e. up to a distance where the solvent density has become uniform (g(r) = 1). In model **II**, on the contrary, the most interacting solvent molecules are included at full QM level, while the remaining solvent is accounted for as a continuum,

$U^{FeRuFe-solv}$	water	methanol	acetonitrile
tot	-1837 ± 65.0	-1259 ± 49	-662 ± 22
Coul	-1757 ± 64.0	-1046 ± 47	-430 ± 21
LJ	-80 ± 27.0	-213 ± 24	-232 ± 17
N_{HB}	30 ± 3	22 ± 2	0

Table 2: Total (*tot*), charge-charge (*Coul*) and LJ **FeRuFe**–solvent interaction energies, computed between **FeRuFe** and all solvent molecules composing the system according to equation (3) and averaged along the 5 ns MD runs. All averages and error estimates are in kJ/mol. The last row reports the number of HBs (N_{HB}) established by **FeRuFe** with each solvent, computed through the standard definition implemented in the GROMACS package.[81]

through PCM. In the latter case, the selection criteria again stand on the solvent structure analysis, and the cut-off radius ($r_{cut}^{QM} = 3.5$Å) is evinced from the radial distribution function obtained from the most interacting atom pairs, e.g. N_z-H_w for the water solvent.

The UV absorption spectra of the **FeRuFe** complex, computed within the CEA-VE scheme along the MD trajectories accounting for water or acetonitrile solvent according to model **I** and **II**, are compared in Figure 9 with the ones obtained with the static model, accounting for the solvent at PCM level. In the following, we first discuss the differences between the spectra calculated according to the different models, and secondly we compare them with the experimental spectra shown in Figure 10. With respect to the gas phase spectrum (which only shows one peak

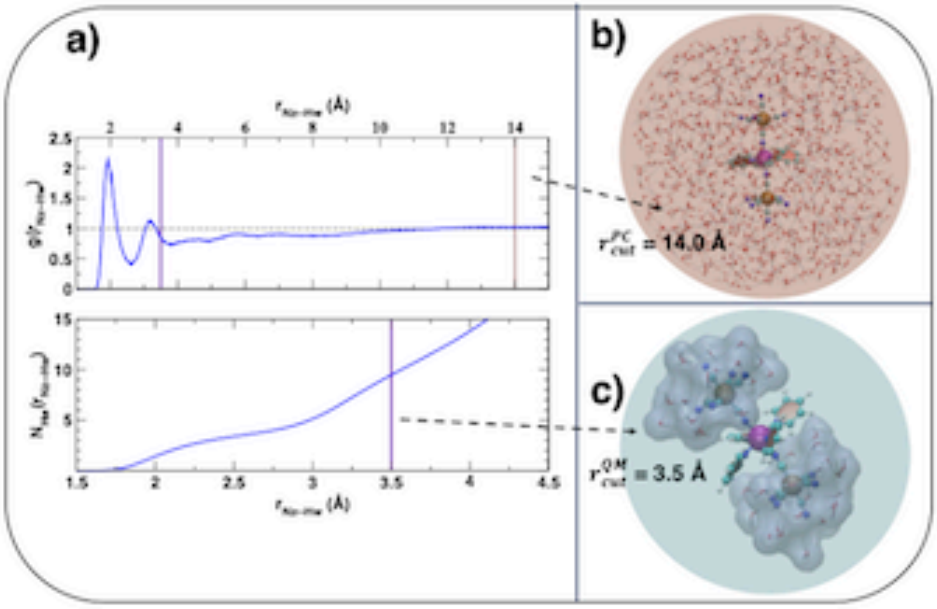

Figure 8: Water solvent models constructed based on radial distribution functions. Panel a): g(r) correlation function between N_z atoms and the water hydrogens (top) corresponding coordination number (bottom). The cut-off radii r_{cut}^{QM} and r_{cut}^{PC}, used in the two adopted solvation models discussed in the text, are shown with shaded purple and brown lines, respectively. Panel b): Pictorial description of the solvent extraction scheme **I**. All water molecules within r_{cut}^{PC} = 14Å with respect the Ru atom are included in the vertical energy calculation as point charges (PC). The resulting solvation sphere is here evidenced with a shaded brown color. Panel c): Model **II**. All water molecules within r_{cut}^{QM} = 3.5Å with respect to any Nz atom (internal shaded surfaces) are included in the vertical energy calculation explicitly at QM level, while the rest of the solvent is accounted at PCM level (bluish sphere).

centered at around 3.5 eV), accounting for the solvent at PCM level results in the appearance of a small peak around 2.7 eV, evidenced upon decreasing the width of the phenomenological Gaussian functions required by the static model from the standard value of 0.33 eV to 0.1 eV (see also Figure S9 in the Supporting Information). Nonetheless, as expected, implicit solvation methods such as PCM fail to distinguish the differences among the two solvents, and the absorption spectra computed in water and MeCN almost coincide. Such a failure can be related both to the conformational dynamics effect of both solute and solvent, missing in the static model, and to the lack of local and specific interactions as HBs, not accounted for by PCM. The importance of the second effect is highlighted in the comparison between the two solvation models based on MD: when mutual solute-solvent polarization effects are well accounted for (i.e. treating the closest molecules at the QM level as in model **II**) the low energy band in water further red shifts (in agreement with the experiment) and the two solvents are well distinguished. For this reason, the final absorption spectra for the three solvents have been computed through the CEA-VE scheme along the MD trajectories with model **II**, and compared with their

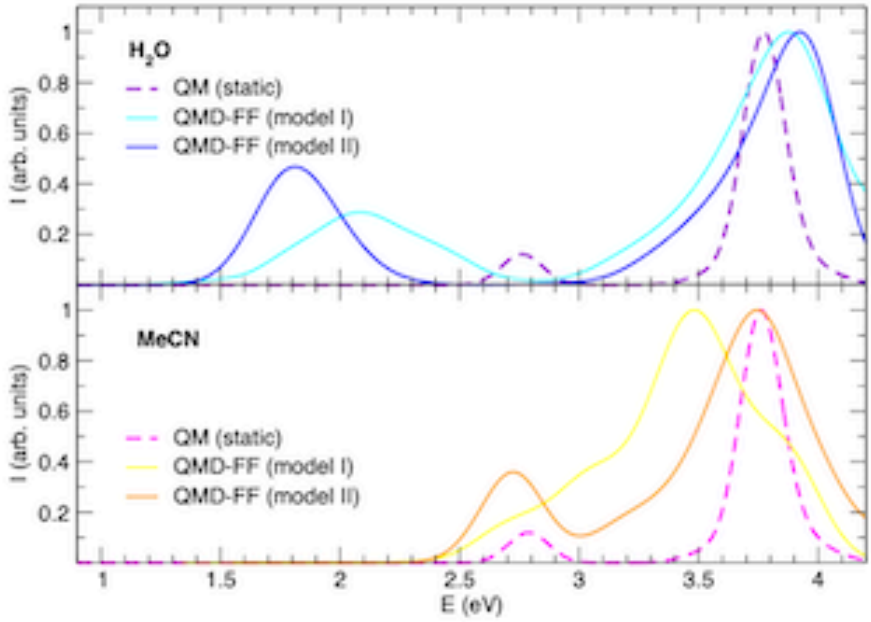

Figure 9: Computed UV absorption spectra of the **FeRuFe** complex, accounting for the water (top) or acetonitrile (bottom) according to the different schemes discussed in the text.

experimental counterparts in Figure 10.

To ease the comparison between the simulated and measured spectra, to match the low energy band registered in water, all computed signals have been red shifted by 0.85 eV. Such an error, also present in the pure QM static approach, can be ascribed to the employed DFT description and it is not related to the parameterized FF. Conversely, the comparison with the experimental spectra over the whole investigated energy range, displayed in the left panels of Figure 10, further confirms the reliability of the QMD-FF, which is able to account for the appearance of a well separated band at low energies, corresponding to the MMCT, correctly red shifted upon increasing polarity and proticity. As evident from the right panels of the same

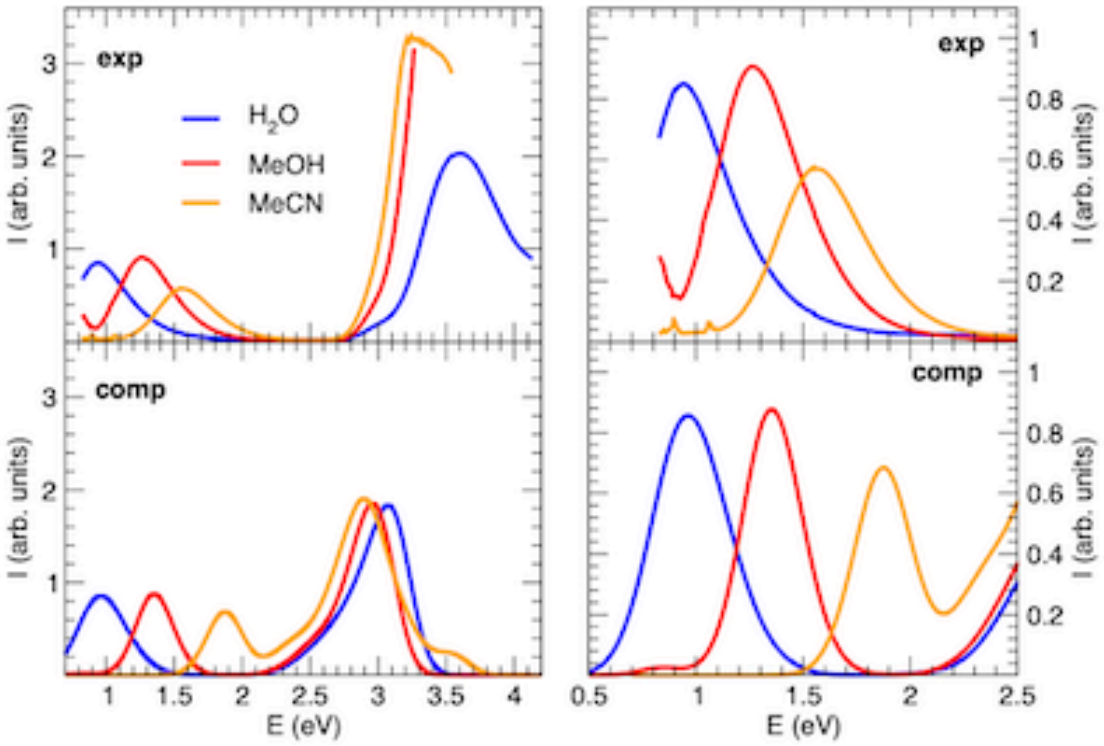

Figure 10: Comparison between experimental (top panels) and computed (bottom panels) UV absorption spectra, registered for the **FeRuFe** complex in different solvents. All calculated spectra are obtained by applying the CEA-VE scheme along the QMD-FF/MD trajectories, accounting for the solvent through model **II**. To ease the comparison, all computed spectra were red-shifted by 0.85 eV.

Figure, the worst agreement among the three solvents is recorded for MeCN. By looking at

the SDFs displayed in Figure 7 and the radial distribution functions in Figure S6, it can be hypothesized that an important role could be played by the dispersion interactions between the electronic density of the solvent cyano groups with the aromatic π cloud of the pyridiyl substituents, which cannot be accounted for by including the solvent molecules surrounding the aromatic ligands only with a continuum. Yet, including also those molecules at QM level (for 100 snapshots) would imply an impressive computational effort, beyond the scope of the present work.

4 Solvent modulation of charge transfer

Deeper insights on the effect of different solvent models on the excited state nature can be obtained by resorting to the excited state charge displacement (ESCD) analysis, developed by some of the authors few years ago.[149,150] This approach is based on the calculation of the function Δq defined as:

$$\Delta q(z) = \int_{-\infty}^{z} dz' \int_{-\infty}^{+\infty} \int_{-\infty}^{+\infty} \Delta\rho(x,y,z')\, dx, dy. \tag{7}$$

where $\Delta\rho(x,y,z)$ represents the electron density difference between the considered excited and ground states. Thus, $\Delta q(z)$ indicates the electron charge that, upon excitation, moves from the right to the left side of the perpendicular plane through the chosen z axis. By definition, when $\Delta q(z)$ is negative the electron is transferred from left to right. This analysis provides a visual indication of the direction and extent of electron transfer over the whole system without resorting to any charge decomposition scheme. We note that the linear **FeRuFe** complex is particularly suitable for this kind of analysis, as the MMCT takes place along the Fe-Ru-Fe (z) axis.

Figure 11 shows the calculated ESCD curves for the lowest-energy MMCT state of a random **FeRuFe** conformation (taken from the MD trajectory in water), either accounting for the three different implicit solvents (top panel) or with the water environment described at different degree of approximation (bottom panel). In line with the observation that in PCM the lowest energy band appears as a weak band centered at about 2.7 eV and is practically overlapped in the three solvents, the ESCD curves plotted in the top panel of Figure 11 indicate that the nature of

the excited state in terms of degree and direction of CT is almost the same in the three implicit media, with a small exception for the most polar water environment. More precisely, for all

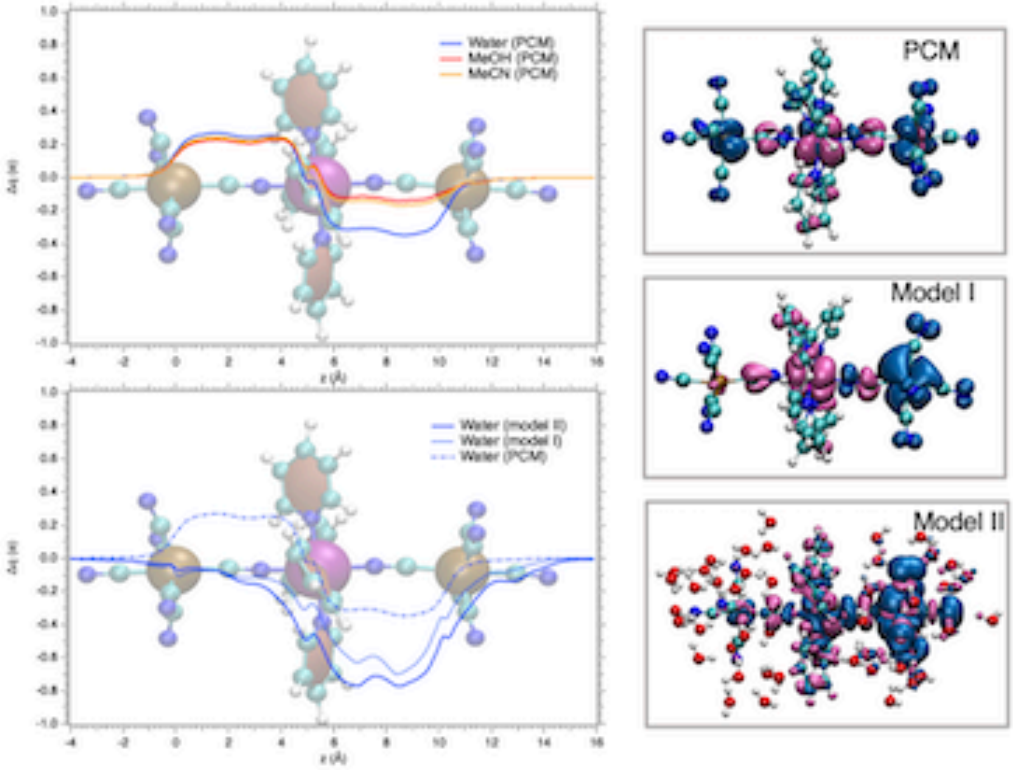

Figure 11: **Left:** ESCD curves of the lowest MMCT state of **FeRuFe** in implicit (PCM) water, methanol and acetonitrile (top panel) and water described by PCM, model **I** an model **II** (bottom panel). For illustrative purposes, a snapshot extracted from the **FeRuFe**@H_2O trajectory has been used in all the ground and excited state electron density calculations to rule out the effects due to change in the solute conformation. The standard "unrelaxed" excited state density has been employed to calculated the density differences.**Right:** Isodensity contour plots of the electron density change in the lowest MMCT state of **FeRuFe** in water by using different solvation schemes. Blue/pink surfaces denote charge accumulation/depletion. The density value at the surfaces is ± 0.001 e$^-$ a.u.$^{-3}$.

the solvents a maximum of 0.25 electrons are transferred from the Ru to the Fe atom on its left (0.23/0.24/0.27 for MeOH/MeCN/water), while toward the Fe on the right 0.14/0.17 e$^-$ move in MeOH/MeCN and 0.35 e$^-$ in water. In PCM, the amount of CT is thus directly proportional to the solvent polarity, and the two "diabatic" $Fe^{II}-Ru^{III}-Fe^{III}$ and $Fe^{III}-Ru^{III}-Fe^{II}$ states turn out to be nearly degenerate and thus weakly interacting.[113] This picture lacks the solvent-cyanide interactions, which are well known to modulate the redox potential of the $Fe^{III/II}$, i.e.

the stability of the diabatic MMCT states, and is clearly inadequate to capture the optical properties of the **FeRuFe** complex.

Conversely, as suggested by the ESCD curves and the associated density difference isodensity plots respectively shown in the bottom left and right panels of Figure 11, when we describe the solvent (water) by point charges (model **I**) or by a QM+PCM scheme (model **II**) the situation is indeed drastically different, in terms of both extent and topology of CT. Already when the electrostatic embedding of the solvent is accounted for by point charges (model **I**), the CT is unidirectional, reaching a maximum value of about 0.7 e^-: this points to of a larger coupling between the two states, resulting in their energy splitting. Interestingly, as apparent in Figure 11, charge depletion starts from the iron center on the left and involves the whole bridge (the axial cyanides, the Ru atom and the pyridines), in agreement with the experimental observation that the electronic communication between the two iron centers is influenced by the nature of the substituents on the pyridine rings.[113] The transferred charge mainly accumulates on the iron center on the right side, as well as on the cyanide N atoms (iron-to-cyanide back bonding). Describing explicitly the first water shell and allowing H-bonding and solvent polarization upon electronic excitation (model **II**), results in an increase of CT (≈ 0.1 electrons) and in a refinement of the discussed picture, as attested by the much more structured density difference plot in the right bottom panel of Figure 11. Charge depletion/accumulation involves the whole $Fe^{III} - CN - Ru^{III}(py)_4 - NC - Fe^{II}(CN)_5$ moiety, as well as the surrounding water molecules closely interacting as HB donors with the terminal cyanide ligands. We note that a meaningful comparison between ESCD curves calculated in different explicit solvents (models **I** and **II**) is not possible because it would require the comparison of results obtained on different snapshots. Finally, if in a simple two state model we take the average energy difference computed in model **II** between the two MMCT states on the 100 snapshots extracted from the MD runs in water and MeCN as a rough estimation of the electronic coupling in the two solvents, we obtain values of 0.05 and 0.03 eV respectively. This confirms, on one hand, that the coupling is larger in the protic and more polar solvent, and, on the other hand, that the degree of electronic communication through the bridge in **FeRuFe** remains moderate for **FeRuFe**, in agreement with the electrochemical data in Ref.[113]

5 Conclusions

We have presented a mixed quantum classical approach, which combines large scale MD simulations, relying on an accurate QMD-FF and self-consistently QM-derived polarized point charges, with IR and UV-Vis spectra calculations to tackle the solvent dependent conformational dynamics and optical properties of a cyano-bridged trinuclear mixed valence compound (**FeRuFe**). Linear cyanide-bridged mixed-valence complexes are prototypical systems to investigate long range ET processes and to elucidate the role played by specific solute-solvent interactions in the modulation of their photophysics. In this perspective, the proposed protocol, applied here to calculate **FeRuFe** ground state properties in water, methanol, and acetonitrile, can be efficiently generalized to calculate transient spectroscopic observables by excited state FF parameterization and non-equilibrium MD simulations.

The accuracy of our classical potential in reliably sampling the **FeRuFe** conformational space and capturing the solute-solvent interactions was first validated by comparing the distribution of selected internal coordinates and the solvent radial distribution functions along the classical MD trajectory with those obtained with a reference QM/MM MD simulation. The resulting agreement allowed us to confidently extend our hybrid protocol to the simulation of **FeRuFe** in different solvents. Interestingly, analysis of the **FeRuFe** dynamics in the three considered media indicates that, while the octahedral structure around the metals is essentially unperturbed by the solvent, the distribution of the flexible dihedrals describing the rotation of the equatorial CN ligands around the CN-Fe-NC axis and the dynamics of the pyridine ligands around the Ru-NC bond is significantly dependent on the its nature (polarity and proticity). A further confirmation of the capability of our QMD-FF in finely describing the H-bonding interactions of protic solvents with the cyanide groups was obtained by comparing the IR vibrational spectra along the MD trajectories in the three solvents with the experimental ones, focusing on the CN stretching mode, being highly sensitive to the H-bonds formation. Calculated IR spectra correctly predicted the red-shift of the CN stretching band in the aprotic medium (MeCN) and the subtle differences measured in water and MeOH.

As far as the Uv-Vis absorption spectra are concerned, we show that a proper comparison

with experiments is possible only when the first solvation shell is explicitly included in the excited state calculations. Implicit solvent models clearly fails in capturing the physics of the photoinduced CT, being indirectly modulated by the solvent-cyanide H-bonds via increase of the electron withdrawing capability of the Fe(II) centers. Inspection of the electron density rearrangements and analysis of the charge displacement excited state curves[149] for the lowest-energy MMCT states demonstrated that, although the electrostatic embedding of the solvent, included by point charges, is able to deliver a notable improvement with respect to PCM in term of CT extent and topology, only by allowing the polarization of the surrounding solvent molecules one can capture the subtle cascade of donating and back-donating effects characterizing the MMCT event. By applying a microsolvation scheme around the Fe-CN moieties and calculating the CEA- VE spectra, the experimental solvatochromic shift was quantitatively reproduced going from water to MeOH.

In conclusion, the present results demonstrate the robustness of our multilevel computational approach, which, thanks to an accurate QMD-FF, capable of exploring a configurational space that is close to that sampled by higher level QM/MM MD, paves the way to large scale (both in terms of in system's size and simulation time) MD simulations of multimetallic mixed valence compounds in different environments. Moreover, the generality of this approach allows its extension to excited states, thus opening the way to the investigation of solute-solvent relaxation dynamics upon ET and BET processes, which can be benchmarked against ultrafast x-ray scattering experiments.[27]

Associated Content
Supporting Information Available

Additional details on intra- and inter- molecular QMD-FF parameterizations, full list of **FeRuFe** QMD-FF parameters, QMD-FF validation tests, additional results concerning solvent structure and absorption Spectra.

Acknowledgments

G.P. thanks the financial support from ICSC – Centro Nazionale di Ricerca in High Performance Computing, Big Data and Quantum Computing, funded by European Union – NextGenerationEU – PNRR, Missione 4 Componente 2 Investimento 1.4. M.P. thanks computational resources from the mésocentre EXPLOR of Université de Lorraine (Project 2018CPMXX0602) and local LPCT resources. E.B., N.G., B.I.P., and M.K. acknowledge support from the U.S. Department of Energy, Office of Science, Office of Basic Energy Sciences, Division of Chemical Sciences, Geosciences, and Biosciences under FWP 80818 at Pacific Northwest National Laboratory (E.B and N.G); DE-SC0019277 and DE-SC0023249 at University of Washington (B.I.P. and M.K.). B.I.P. also acknowledges support from the NSF GRFP (No. DGE-1762114). This research also benefited from computational resources provided by EMSL, a DOE Office of Science User Facility sponsored by the Office of Biological and Environmental Research and located at PNNL. PNNL is operated by Battelle Memorial Institute for the United States Department of Energy under DOE Contract No. DE-AC05-76RL1830. Computational resources provided by the National Energy Research Scientific Computing Center (NERSC), a U.S. Department of Energy Office of Science User Facility operated under Contract No. DE-AC02-05CH11231 are also gratefully acknowledged. This research used resources of the Stanford Synchrotron Radiation Lightsource (SSRL) at SLAC National Accelerator Laboratory. SSRL is supported by the U.S. Department of Energy, Office of Science, Office of Basic Energy Sciences under Contract No. DE-AC02-76SF00515.

References

[1] D'Alessandro, D. M.; Keene, F. R. Current trends and future challenges in the experimental, theoretical and computational analysis of intervalence charge transfer (IVCT) transitions *Chem. Soc. Rev.* **2006**, *35*, 424–440.

[2] D'Alessandro, D. M.; Keene, F. R. Intervalence Charge Transfer (IVCT) in Trinuclear and Tetranuclear Complexes of Iron, Ruthenium, and Osmium *Chem. Rev.* **2006**, *106*, 2270–2298.

[3] Barbara, P. F.; Meyer, T. J.; Ratner, M. A. Contemporary Issues in Electron Transfer Research *J. Phys. Chem.* **1996**, *100*, 13148–13168.

[4] Balzani, V.; Juris, A.; Venturi, M.; Campagna, S.; Serroni, S. Luminescent and Redox-Active Polynuclear Transition Metal Complexes *Chem. Rev.* **1996**, *96*, 759–834.

[5] Scandola, F.; Argazzi, R.; Bignozzi, C.; Chiorboli, C.; Indelli, M.; Rampi, M. Electronic coupling between remote metal centers in cyanobridged polynuclear complexes *Coord. Chem. Rev.* **1993**, *125*, 283–292.

[6] Bernhardt, P. V.; Bozoglián, F.; Macpherson, B. P.; Martínez, M. Molecular mixed-valence cyanide bridged CoIII - FeII complexes *Coord. Chem. Rev.* **2005**, *249*, 1902–1916; 36th International Conference on Coordination Chemistry, Merida, Mexico, July 2004.

[7] Alborés, P.; Rossi, M. B.; Baraldo, L. M.; Slep, L. D. Donor-Acceptor Interactions and Electron Transfer in Cyano-Bridged Trinuclear Compounds *Inorg. Chem.* **2006**, *45*, 10595–10604.

[8] Manor, B. C.; Rauchfuss, T. B. Hydrogen Activation by Biomimetic [NiFe]-Hydrogenase Model Containing Protected Cyanide Cofactors *Journal of the American Chemical Society* **2013**, *135*, 11895–11900.

[9] Wang, H.-Y.; Wang, W.-G.; Si, G.; Wang, F.; Tung, C.-H.; Wu, L.-Z. Photocatalytic Hydrogen Evolution from Rhenium(I) Complexes to [FeFe] Hydrogenase Mimics in Aqueous SDS Micellar Systems: A Biomimetic Pathway *Langmuir* **2010**, *26*, 9766–9771.

[10] Cook, T. R.; Zheng, Y.-R.; Stang, P. J. Metal–Organic Frameworks and Self-Assembled Supramolecular Coordination Complexes: Comparing and Contrasting the Design, Synthesis, and Functionality of Metal–Organic Materials *Chemical Reviews* **2013**, *113*, 734–777.

[11] Wang, F.; Wang, W.-G.; Wang, H.-Y.; Si, G.; Tung, C.-H.; Wu, L.-Z. Artificial Photosynthetic Systems Based on [FeFe]-Hydrogenase Mimics: the Road to High Efficiency for Light-Driven Hydrogen Evolution *ACS Catalysis* **2012**, *2*, 407–416.

[12] Caserta, G.; Roy, S.; Atta, M.; Artero, V.; Fontecave, M. Artificial hydrogenases: biohybrid and supramolecular systems for catalytic hydrogen production or uptake *Current Opinion in Chemical Biology* **2015**, *25*, 36–47.

[13] Liu, T.; Dong, D.-P.; Kanegawa, S.; Kang, S.; Sato, O.; Shiota, Y.; Yoshizawa, K.; Hayami, S.; Wu, S.; He, C.; Duan, C.-Y. Reversible Electron Transfer in a Linear Fe2Co Trinuclear Complex Induced by Thermal Treatment and Photoirraditaion *Angewandte Chemie International Edition* **2012**, *51*, 4367–4370.

[14] Bernhardt, P. V.; Boschloo, G. K.; Bozoglian, F.; Hagfeldt, A.; Martínez, M.; Sienra, B. Tailoring mixed-valence CoIII/FeII complexes for their potential use as sensitizers in dye sensitized solar cells *New J. Chem.* **2008**, *32*, 705–711.

[15] Manbeck, G. F.; Brewer, K. J. Photoinitiated electron collection in polyazine chromophores coupled to water reduction catalysts for solar H2 production *Coord. Chem. Rev.* **2013**, *257*, 1660–1675.

[16] Yamada, Y.; Yoneda, M.; Fukuzumi, S. High Power Density of One-Compartment H2O2 Fuel Cells Using Pyrazine-Bridged Fe[MC(CN)4] (MC = Pt2+ and Pd2+) Complexes as the Cathode *Inorganic Chemistry* **2014**, *53*, 1272–1274.

[17] Aratani, Y.; Oyama, K.; Suenobu, T.; Yamada, Y.; Fukuzumi, S. Photocatalytic Hydroxylation of Benzene by Dioxygen to Phenol with a Cyano-Bridged Complex Containing FeII and RuII Incorporated in Mesoporous Silica–Alumina *Inorg. Chem.* **2016**, *55*, 5780–5786.

[18] Okubo, M.; Kagesawa, K.; Mizuno, Y.; Asakura, D.; Hosono, E.; Kudo, T.; Zhou, H.; Fujii, K.; Uekusa, H.; Nishimura, S.-i.; Yamada, A.; Okazawa, A.; Kojima, N. Reversible Solid State Redox of an Octacyanometallate-Bridged Coordination Polymer by Electrochemical Ion Insertion/Extraction *Inorg. Chem.* **2013**, *52*, 3772–3779.

[19] Goberna-Ferrón, S.; Hernández, W. Y.; Rodríguez-García, B.; Galán-Mascarós, J. R. Light-Driven Water Oxidation with Metal Hexacyanometallate Heterogeneous Catalysts *ACS Catal.* **2014**, *4*, 1637–1641.

[20] Nemykin, V. N.; Purchel, A. A.; Spaeth, A. D.; Barybin, M. V. Probing the Electronic Properties of a Trinuclear Molecular Wire Involving Isocyanoferrocene and Iron(II) Phthalocyanine Motifs *Inorg. Chem.* **2013**, *52*, 11004–11012.

[21] Tanaka, Y.; Kato, Y.; Sugimoto, K.; Kawano, R.; Tada, T.; Fujii, S.; Kiguchi, M.; Akita, M. Single-molecule junctions of multinuclear organometallic wires: long-range carrier transport brought about by metal–metal interaction *Chem. Sci.* **2021**, *12*, 4338–4344.

[22] Courtney, T. L.; Fox, Z. W.; Estergreen, L.; Khalil, M. Measuring Coherently Coupled Intramolecular Vibrational and Charge-Transfer Dynamics with Two-Dimensional Vibrational–Electronic Spectroscopy *J. Phys. Chem. Lett.* **2015**, *6*, 1286–1292.

[23] Courtney, T. L.; Fox, Z. W.; Slenkamp, K. M.; Khalil, M. Two-dimensional vibrational-electronic spectroscopy *J. Chem. Phys.* **2015**, *143*, 154201.

[24] Tominaga, K.; Kliner, D. A. V.; Johnson, A. E.; Levinger, N. E.; Barbara, P. F. Femtosecond experiments and absolute rate calculations on intervalence electron transfer of mixed-valence compounds *J. Chem. Phys.* **1993**, *98*, 1228–1243.

[25] Vance, F. W.; Slone, R. V.; Stern, C. L.; Hupp, J. T. Comparative absorption, electroabsorption and electrochemical studies of intervalence electron transfer and electronic coupling in cyanide-bridged bimetallic systems: ancillary ligand effects *Chem. Phys.* **2000**, *253*, 313–322.

[26] Van Kuiken, B. E.; Valiev, M.; Daifuku, S. L.; Bannan, C.; Strader, M. L.; Cho, H.; Huse, N.; Schoenlein, R. W.; Govind, N.; Khalil, M. Simulating Ru L3-Edge X-ray Absorption Spectroscopy with Time-Dependent Density Functional Theory: Model Complexes and Electron Localization in Mixed-Valence Metal Dimers *J. Phys. Chem. AVanKuiken2013* **2013**, *117*, 4444–4454.

[27] Biasin, E.; Fox, Z. W.; Andersen, A.; Ledbetter, K.; Kjær, K. S.; Alonso-Mori, R.; Carlstad, J. M.; Chollet, M.; Gaynor, J. D.; Glownia, J. M.; Hong, K. ; Kroll, T. ; Lee, J. H- ; Liekhus-Schmaltz, C. ; Reinhard, M. ; Sokaras, D. ; Zhang, Y. ; Doumy, G. ; March, A. M. ; Southworth, S. H. ; Mukamel, S. ; Gaffney, K. J. ; Schoenlein, R. W. ; Govind, N. ; Cordones, A. A. ; Khalil, M. Direct observation of coherent femtosecond solvent reorganization coupled to intramolecular electron transfer *Nat. Chem.* **2021**, *13*, 343–349.

[28] Reid, P. J.; Silva, C.; Barbara, P. F.; Karki, L.; Hupp, J. T. Electronic coherence, vibrational coherence, and solvent degrees of freedom in the femtosecond spectroscopy of mixed-valence metal dimers in H2O and D2O *J. Phys. Chem.* **1995**, *99*, 2609–2616.

[29] Toma, H. E.; Takasugi, M. S. Spectroscopic studies of preferential and asymmetric solvation in substituted cyanoiron (II) complexes *J. Sol. Chem.* **1983**, *12*, 547–561.

[30] Linert, W.; Gutmann, V. Structural and electronic responses of coordination compounds to changes in the molecule and molecular environment *Coord. Chem. Rev.* **1992**, *117*, 159–183.

[31] Georgieva, I.; Aquino, A. J.; Trendafilova, N.; Santos, P. S.; Lischka, H. Solvatochromic and Ionochromic Effects of Iron (II) bis (1, 10-phenanthroline) dicyano: a Theoretical Study *Inorg. Chem.* **2010**, *49*, 1634–1646.

[32] Timpson, C. J.; Bignozzi, C. A.; Sullivan, B. P.; Kober, E. M.; Meyer, T. J. Influence of solvent on the spectroscopic properties of cyano complexes of ruthenium (II) *J. Phys. Chem.* **1996**, *100*, 2915–2925.

[33] Davies, G. M.; Pope, S. J.; Adams, H.; Faulkner, S.; Ward, M. D. Structural and photophysical properties of coordination networks combining [Ru (bipy)(CN) 4] 2-anions and lanthanide (III) cations: rates of photoinduced Ru-to-lanthanide energy transfer and sensitized near-infrared luminescence *Inorg. Chem.* **2005**, *44*, 4656–4665.

[34] Indelli, M.; Ghirotti, M.; Prodi, A.; Chiorboli, C.; Scandola, F.; McClenaghan, N.; Puntoriero, F.; Campagna, S. Solvent switching of intramolecular energy transfer in bichromophoric systems: Photophysics of (2, 2 '-Bipyridine) tetracyanoruthenate (II)/pyrenyl complexes *Inorg. Chem.* **2003**, *42*, 5489–5497.

[35] Zederkof, D. B.; Møller, K. B.; Nielsen, M. M.; Haldrup, K.; González, L.; Mai, S. Resolving Femtosecond Solvent Reorganization Dynamics in an Iron Complex by Nonadiabatic Dynamics Simulations *J. Am. Chem. Soc.* **2022**, *144*, 12861–12873.

[36] Kjær, K. S.; Kunnus, K.; Harlang, T. C. B.; Van Driel, T. B.; Ledbetter, K.; Hartsock, R. W.; Reinhard, M. E.; Koroidov, S.; Li, L.; Laursen, M. G.; Biasin, E.; Hansen, F. B.; Vester, P.; Christensen, M.; Haldrup, K.; Nielsen, M. M.; Chabera, P.; Liu, Y.; Tatsuno, H.; Timm, C.; Uhlig, J.; Sundstöm, V.; Németh, Z.; Szemes, D. S.; Bajnóczi, É.; Vankó, G.; Alonso-Mori, R.; Glownia, J. M.; Nelson, S.; Sikorski, M.; Sokaras, D.; Lemke, H. T.; Canton, S. E.; Wärnmark, K.; Persson, P.; Cordones, A. A.; Gaffney, K. J. Solvent control of charge transfer excited state relaxation pathways in [Fe(2,2′-bipyridine)$(CN)_4]^{2-}$ *Phys. Chem. Chem. Phys.* **2018**, *20*, 4238–4249.

[37] Kunnus, K.; Li, L.; Titus, C. J.; Lee, S. J.; Reinhard, M. E.; Koroidov, S.; Kjær, K. S.; Hong, K.; Ledbetter, K.; Doriese, W. B.; O'Neil, G. C.; Swetz, D. S.; Ullom, J. N.; Li, D.; Irwin, K.; Nordlund, D.; Cordones, A. A.; Gaffney, K. J. Chemical control of competing electron transfer pathways in iron tetracyano-polypyridyl photosensitizers *Chem. Sci.* **2020**, *11*, 4360–4373.

[38] Taft, R.; Pienta, N. J.; Kamlet, M. J.; Arnett, E. M. Linear solvation energy relationships. 7. Correlations between the solvent-donicity and acceptor-number scales and the solvatochromic parameters. pi.*,. alpha., and. beta. *J. Org. Chem.* **1981**, *46*, 661–667.

[39] Tavernelli, I.; Curchod, B. F.; Rothlisberger, U. Nonadiabatic molecular dynamics with solvent effects: A LR-TDDFT QM/MM study of ruthenium (II) tris (bipyridine) in water *Chem. Phys.* **2011**, *391*, 101–109.

[40] Mai, S.; González, L. Unconventional two-step spin relaxation dynamics of [Re (CO) 3 (im)(phen)]+ in aqueous solution *Chem. Sci.* **2019**, *10*, 10405–10411.

[41] Fang, Y.-G.; Peng, L.-Y.; Liu, X.-Y.; Fang, W.-H.; Cui, G. QM/MM nonadiabatic dynamics simulation on ultrafast excited-state relaxation in osmium (II) compounds in solution *Comput. Theor. Chem.* **2019**, *1155*, 90–100.

[42] Prampolini, G.; Ingrosso, F.; Segalina, A.; Caramori, S.; Foggi, P.; Pastore, M. Dynamical and Environmental Effects on the Optical Properties of an Heteroleptic Ru(II)–Polypyridine Complex: A Multilevel Approach Combining Accurate Ground and Excited State QM-Derived Force Fields, MD and TD-DFT *J. Chem. Theory Comput.* **2019**, *15*, 529–545.

[43] Prampolini, G.; Ingrosso, F.; Cerezo, J.; Iagatti, A.; Foggi, P.; Pastore, M. Short- and Long-Range Solvation Effects on the Transient UV–Vis Absorption Spectra of a Ru(II)–Polypyridine Complex Disentangled by Nonequilibrium Molecular Dynamics *J. Phys. Chem. Lett.* **2019**, *10*, 2885–2891.

[44] Diez-Cabanes, V.; Prampolini, G.; Francés-Monerris, A.; Monari, A.; Pastore, M. Iron's Wake: The Performance of Quantum Mechanical-Derived Versus General-Purpose Force Fields Tested on a Luminescent Iron Complex *Molecules* **2020**, *25*.

[45] Zulfikri, H.; Pápai, M.; Dohn, A. O. Simulating the solvation structure of low- and high-spin [Fe(bpy)3]2+: long-range dispersion and many-body effects *Phys. Chem. Chem. Phys.* **2022**, *24*, 16655–16670.

[46] Smith, J. S.; Isayev, O.; Roitberg, A. E. ANI-1: an extensible neural network potential with DFT accuracy at force field computational cost *Chem. Sci.* **2017**, *8*, 3192–3203.

[47] Gastegger, M.; Behler, J.; Marquetand, P. Machine learning molecular dynamics for the simulation of infrared spectra *Chem. Sci.* **2017**, *8*, 6924–6935.

[48] Botu, V.; Ramprasad, R. Adaptive machine learning framework to accelerate ab initio molecular dynamics *Int. J. Quant. Chem.* **2015**, *115*, 1074–1083.

[49] Moret, M.-E.; Tavernelli, I.; Rothlisberger, U. Combined QM/MM and Classical Molecular Dynamics Study of [Ru(bpy) ₃] ²⁺ in Water *J. Phys. Chem. B* **2009**, *113*, 7737–7744.

[50] Moret, M.-E.; Tavernelli, I.; Chergui, M.; Rothlisberger, U. Electron Localization Dynamics in the Triplet Excited State of [Ru(bpy) ₃] ²⁺ in Aqueous Solution *Chem. Eur. J.* **2010**, *16*, 5889–5894.

[51] Mosconi, E.; Azpiroz, J. M.; De Angelis, F. Ab Initio Molecular Dynamics Simulations of Methylammonium Lead Iodide Perovskite Degradation by Water *Chem. Mater.* **2015**, *27*, 4885–4892.

[52] Ko, H.-Y.; Jia, J.; Santra, B.; Wu, X.; Car, R.; DiStasio Jr, R. A. Enabling large-scale condensed-phase hybrid density functional theory based ab initio molecular dynamics. 1. theory, algorithm, and performance *J. Chem. theor. Comput.* **2020**, *16*, 3757–3785.

[53] Ang, S. J.; Wang, W.; Schwalbe-Koda, D.; Axelrod, S.; Gómez-Bombarelli, R. Active learning accelerates ab initio molecular dynamics on reactive energy surfaces *Chem* **2021**, *7*, 738–751.

[54] Seritan, S.; Bannwarth, C.; Fales, B. S.; Hohenstein, E. G.; Isborn, C. M.; Kokkila-Schumacher, S. I.; Li, X.; Liu, F.; Luehr, N.; Snyder Jr, J. W.; Song, C. ; Titov, A. V. ; Ufimtsev, I. S. Wang, L.-P. ; Martínez, T. J., TeraChem: A graphical processing unit-accelerated electronic structure package for large-scale ab initio molecular dynamics *Wiley Interdiscip. Rev. Comput. Mol. Sci.* **2021**, *11*, e1494.

[55] Schade, R.; Kenter, T.; Elgabarty, H.; Lass, M.; Schütt, O.; Lazzaro, A.; Pabst, H.; Mohr, S.; Hutter, J.; Kühne, T. D.; Plessl, C. Towards electronic structure-based ab-initio molecular dynamics simulations with hundreds of millions of atoms *Parallel Comput.* **2022**, *111*, 102920.

[56] Gaillac, R.; Pullumbi, P.; Bennett, T. D.; Coudert, F.-X. Structure of metal–organic framework glasses by ab initio molecular dynamics *Chem. Mater.* **2020**, *32*, 8004–8011.

[57] Segalina, A.; Lebègue, S.; Rocca, D.; Piccinin, S.; Pastore, M. Structure and Energetics of Dye-Sensitized NiO Interfaces in Water from Ab Initio MD and Large-Scale GW Calculations *J. Chem. Theor. Comput.* **2021**, *17*, 5225–5238.

[58] He, L.; Guo, Y.; Kloo, L. Insights into the Explicit Mechanism and Dynamic Rate of Regeneration of Sensitizing Organic Dyes by Transition-Metal Redox Mediators in Solar Cells Using Ab Initio Molecular Dynamics *ACS Appl. En. Mater.* **2022**.

[59] Morzan, U. N.; Alonso de Armino, D. J.; Foglia, N. O.; Ramírez, F.; González Lebrero, M. C.; Scherlis, D. A.; Estrin, D. A. Spectroscopy in Complex Environments from QM–MM Simulations *Chem. Rev.* **2018**, *118*, 4071–4113.

[60] Vennelakanti, V.; Nazemi, A.; Mehmood, R.; Steeves, A. H.; Kulik, H. J. Harder, better, faster, stronger: Large-scale QM and QM/MM for predictive modeling in enzymes and proteins *Curr. Opin. Struct. Biol.* **2022**, *72*, 9–17.

[61] Taylor, M.; Yu, H.; Ho, J. Predicting Solvent Effects on SN2 Reaction Rates: Comparison of QM/MM, Implicit, and MM Explicit Solvent Models *J. Phys. Chem. B* **2022**, *126*, 9047–9058.

[62] Li, P.; Rangadurai, A.; Al-Hashimi, H. M.; Hammes-Schiffer, S. Environmental effects on guanine-thymine mispair tautomerization explored with quantum mechanical/molecular mechanical free energy simulations *J. Am. Chem. Soc.* **2020**, *142*, 11183–11191.

[63] Sen, S.; Kar, R. K.; Borin, V. A.; Schapiro, I. Insight into the isomerization mechanism of retinal proteins from hybrid quantum mechanics/molecular mechanics simulations *Wiley Interdiscip. Rev. Comput. Mol. Sci.* **2022**, *12*, e1562.

[64] Abedi, M.; Levi, G.; Zederkof, D. B.; Henriksen, N. E.; Pápai, M.; Møller, K. B. Excited-state solvation structure of transition metal complexes from molecular dynamics simulations and assessment of partial atomic charge methods *Phys. Chem. Chem. Phys.* **2019**, *21*, 4082–4095.

[65] Ross, M.; Andersen, A.; Fox, Z. W.; Zhang, Y.; Hong, K.; Lee, J.-H.; Cordones, A.; March, A. M.; Doumy, G.; Southworth, S. H.; Marcus, M. A. ; Schoenlein, R. W. ; Mukamel, S. ; Govind, N. ; Khalil, M. Comprehensive experimental and computational spectroscopic study of hexacyanoferrate complexes in water: From infrared to X-ray wavelengths *J. Phys. Chem. B* **2018**, *122*, 5075–5086.

[66] March, A.; Doumy, G.; Andersen, A.; Al Haddad, A.; Kumagai, Y.; Tu, M.; Bang, J.; Bostedt, C.; Uhlig, J.; Nascimento, D.; et al. ; Assefa, T. A. ; Németh, Z. and Vankó, G. ; Gawelda, W. ; Govind, N. ; Young, L. Elucidation of the photoaquation reaction mechanism in ferrous hexacyanide using synchrotron x-rays with sub-pulse-duration sensitivity. *J. Phys. Chem. B* **2019**, *151*, 144306–144306.

[67] Böselt, L.; Thürlemann, M.; Riniker, S. Machine Learning in QM/MM Molecular Dynamics Simulations of Condensed-Phase Systems *J. Chem. Theor. Comput.* **2021**, *17*, 2641–2658.

[68] Lier, B.; Poliak, P.; Marquetand, P.; Westermayr, J.; Oostenbrink, C. BuRNN: Buffer Region Neural Network Approach for Polarizable-Embedding Neural Network/Molecular Mechanics Simulations *J. Phys. Chem. Lett.* **2022**, *13*, 3812–3818; PMID: 35467875.

[69] Zeng, J.; Giese, T. J.; Ekesan, S.; York, D. M. Development of range-corrected deep learning potentials for fast, accurate quantum mechanical/molecular mechanical simulations of chemical reactions in solution *J. Chem. Theor. Comput.* **2021**, *17*, 6993–7009.

[70] Allen, M. P.; Tildesley, D. J. Computer Simulation of Liquids; Clarendon: Oxford, 1987.

[71] Frenkel, D.; Smith, B. Understanding Molecular Simulations; Academic Press: San Diego, 1996.

[72] Hansen, N.; van Gunsteren, W. F. Practical Aspects of Free-Energy Calculations: A Review *J. Chem. Theory Comput.* **2014**, *10*, 2632–2647.

[73] Riniker, S. Fixed-Charge Atomistic Force Fields for Molecular Dynamics Simulations in the Condensed Phase: An Overview *J. Chem. Inf. Mod.* **2018**, *58*, 565–578.

[74] König, G.; Riniker, S. On the faithfulness of molecular mechanics representations of proteins towards quantum-mechanical energy surfaces *Interface Focus* **2020**, *10*, 20190121.

[75] Csizi, K.-S.; Reiher, M. Universal QM/MM approaches for general nanoscale applications *WIREs Comp. Mole. Sci.* **2022**, *doi:https://doi.org/10.1002/wcms.1656*.

[76] Rappe, A. K.; Casewit, C. J.; Colwell, K. S.; Goddard, W. A.; Skiff, W. M. UFF, a full periodic table force field for molecular mechanics and molecular dynamics simulations *J. Am. Chem. Soc.* **1992**, *114*, 10024–10035.

[77] Jorgensen, W. L.; Maxwell, D. S.; Tirado-rives, J. Development and Testing of the OPLS All-Atom Force Field on Conformational Energetics and Properties of Organic Liquids *J. Am. Chem. Soc.* **1996**, *7863*, 11225–11236.

[78] Jorgensen, W. L.; Tirado-Rives, J. Potential Energy Functions for Atomic-Level Simulations of Water and Organic and Biomolecular Systems. *Proc. Natl. Acad. Sci. USA* **2005**, *102*, 6665–70.

[79] Bonomi, M.; Camilloni, C. Biomolecular Simulations; Methods in Molecular Biology, Vol. 2022; Springer: New York, 2019.

[80] Case, D. A.; Cheatham, T. E.; Darden, T.; Gohlke, H.; Luo, R.; Merz, K. M.; Onufriev, A.; Simmerling, C.; Wang, B.; Woods, R. J. The Amber biomolecular simulation programs *J. Comp. Chem.* **2005**, *26*, 1668–1688.

[81] Pronk, S.; Páll, S.; Schulz, R.; Larsson, P.; Bjelkmar, P.; Apostolov, R.; Shirts, M. R.; Smith, J. C.; Kasson, P. M.; van der Spoel, D.; Hess, B.; Lindahl, E. GROMACS 4.5: a High-Throughput and Highly Parallel Open Source Molecular Simulation Toolkit *Bioinformatics* **2013**, *29*, 845–854.

[82] Thompson, A. P.; Aktulga, H. M.; Berger, R.; Bolintineanu, D. S.; Brown, W. M.; Crozier, P. S.; in 't Veld, P. J.; Kohlmeyer, A.; Moore, S. G.; Nguyen, T. D.; Shan, R.; Stevens, M. J.; Tranchida, J.; Trott, C.; Plimpton, S. J. LAMMPS - a flexible simulation tool for particle-based materials modeling at the atomic, meso, and continuum scales *Comp. Phys. Comm.* **2022**, *271*, 108171.

[83] Phillips, J. C.; Hardy, D. J.; Maia, J. D. C.; Stone, J. E.; Ribeiro, J. V.; Bernardi, R. C.; Buch, R.; Fiorin, G.; Hénin, J.; Jiang, W.; McGreevy, R.; Melo, M. C. R.; Radak, B. K.; Skeel, R. D.; Singharoy, A.; Wang, Y.; Roux, B.; Aksimentiev, A.; Luthey-Schulten, Z.; Kalé, L. V.; Schulten, K.; Chipot, C.; Tajkhorshid, E. Scalable molecular dynamics on CPU and GPU architectures with NAMD *J. Chem. Phys.* **2020**, *153*, 044130.

[84] Brooks, B. R.; Brooks, C. L.; Mackerell, A. D.; Nilsson, L.; Petrella, R. J.; Roux, B.; Won, Y.; Archontis, G.; Bartels, C.; Boresch, S.; Caflisch, A.; Caves, L.; Cui, Q.; Dinner, A. R.; Feig, M.; Fischer, S.; Gao, J.; Hodoscek, M.; Im, W.; Kuczera, K.; Lazaridis, T.; Ma, J.; Ovchinnikov, V.; Paci, E.; Pastor, R. W.; Post, C. B.; Pu, J. Z.; Schaefer, M.; Tidor, B.; Venable, R. M.; Woodcock, H. L.; Wu, X.; Yang, W.; York, D. M.; Karplus, M. CHARMM: The biomolecular simulation program *J. Comp. Chem.* **2009**, *30*, 1545–1614.

[85] Rackers, J. A.; Wang, Z.; Lu, C.; Laury, M. L.; Lagardère, L.; Schnieders, M. J.; Piquemal, J.-P.; Ren, P.; Ponder, J. W. Tinker 8: software tools for molecular design *J. Chem. Theor. Comput.* **2018**, *14*, 5273–5289.

[86] Li, P.; Merz Jr, K. M. Metal ion modeling using classical mechanics *Chem. Rev.* **2017**, *117*, 1564–1686.

[87] Lunghi, A.; Sanvito, S. A unified picture of the covalent bond within quantum-accurate force fields: From organic molecules to metallic complexes' reactivity *Sci. Adv.* **2019**, *5*, eaaw2210.

[88] Mennucci, B. Modeling absorption and fluorescence solvatochromism with QM/Classical approaches *Int. J. Quant. Chem.* **2015**, *18*, 1202–1208.

[89] Cacelli, I.; Cinacchi, G.; Prampolini, G.; Tani, A. Computer Simulation of Solid and Liquid Benzene with an Atomistic Interaction Potential Derived from Ab Initio Calculations. *J. Am. Chem. Soc.* **2004**, *126*, 14278–86.

[90] Cacelli, I.; Prampolini, G. Parametrization and Validation of Intramolecular Force Fields Derived from DFT Calculations *J. Chem. Theory Comput.* **2007**, *3*, 1803–1817.

[91] Cacelli, I.; Cimoli, A.; Livotto, P. R.; Prampolini, G. An Automated Approach for the Parameterization of Accurate Intermolecular Force-Fields: Pyridine as a Case Study. *J. Comp. Chem.* **2012**, *33*, 1055.

[92] Piquemal, J.-P.; Jordan, K. D. From Quantum Mechanics to Force Fields: New Methodologies for the Classical Simulation of Complex Systems *Theor. Chem. Accounts* **2012**, *131*, 1207.

[93] Bureekaew, S.; Amirjalayer, S.; Tafipolsky, M.; Spickermann, C.; Roy, T. K.; Schmid, R. MOF-FF - A flexible first-principles derived force field for metal-organic frameworks *Phys. Status Solidi B* **2013**, *250*, 1128–1141.

[94] Grimme, S. A General Quantum Mechanically Derived Force Field (QMDFF) for Molecules and Condensed Phase Simulations *J. Chem. Theory Comput.* **2014**, 4497–4514.

[95] Prampolini, G.; Livotto, P. R.; Cacelli, I. Accuracy of Quantum Mechanically Derived Force-Fields Parameterized from Dispersion-Corrected DFT Data: The Benzene Dimer as a Prototype for Aromatic Interactions. *J. Chem. Theory Comput.* **2015**, *11*, 5182–96.

[96] Vanduyfhuys, L.; Vandenbrande, S.; Verstraelen, T.; Schmid, R.; Waroquier, M.; Van Speybroeck, V. QuickFF: A Program for a Quick and Easy Derivation of Force Fields for Metal-Organic Frameworks from Ab Initio Input. *J. Chem. Theory Comput.* **2015**, *36*, 1015–27.

[97] Bristow, J. K.; Skelton, J. M.; Svane, K. L.; Walsh, A.; Gale, J. D. A general forcefield for accurate phonon properties of metal–organic frameworks *Phys. Chem. Chem. Phys.* **2016**, *18*, 29316–29329.

[98] Piquemal, J.-p.; Jordan, K. D. Preface: Special Topic: From Quantum Mechanics to Force Fields *J. Chem. Phys.* **2017**, *147*, 161401.

[99] Vanduyfhuys, L.; Vandenbrande, S.; Wieme, J.; Waroquier, M.; Verstraelen, T.; Van Speybroeck, V. Extension of the QuickFF force field protocol for an improved accuracy of structural, vibrational, mechanical and thermal properties of metal–organic frameworks *J. Comp. Chem.* **2018**, *39*, 999–1011.

[100] Claridge, K.; Troisi, A. Developing Consistent Molecular Dynamics Force Fields for Biological Chromophores via Force Matching *J. Phys. Chem. B* **2019**, *123*, 428–438.

[101] Horton, J. T.; Allen, A. E. A.; Dodda, L. S.; Cole, D. J. QUBEKit: Automating the Derivation of Force Field Parameters from Quantum Mechanics *J. Chem. Inf. Mod.* **2019**, *59*, 1366–1381.

[102] Santos, L. d. A.; Prandi, I. G.; Ramalho, T. C. Could Quantum Mechanical Properties Be Reflected on Classical Molecular Dynamics? The Case of Halogenated Organic Compounds of Biological Interest *Frontiers in Chemistry* **2019**, *7*, 1–10.

[103] Odinokov, A.; Yakubovich, A.; Son, W.-j.; Jung, Y.; Choi, H. Exploiting the quantum mechanically derived force field for functional materials simulations *Comput. Mat.* **2021**, *7*, 155.

[104] Vilhena, J.; Greff da Silveira, L.; Livotto, P. R.; Cacelli, I.; Prampolini, G. Automated Parameterization of Quantum Mechanically Derived Force Fields for Soft Materials and

Complex Fluids: Development and Validation *J. Chem. Theory Comput.* **2021**, *17*, 4449–4464.

[105] Yang, L.; Horton, J. T.; Payne, M. C.; Penfold, T. J.; Cole, D. J. Modeling Molecular Emitters in Organic Light-Emitting Diodes with the Quantum Mechanical Bespoke Force Field *J. Chem. Theory Comput.* **2021**, *17*, 5021–5033.

[106] Prampolini, G.; Silveira, L. G. D.; Vilhena, J. G.; Livotto, P. R. Predicting Spontaneous Orientational Self-Assembly: In Silico Design of Materials with Quantum Mechanically Derived Force Fields *J. Phys. Chem. Lett.* **2022**, *13*, 243–250.

[107] da Silveira, L. G.; Livotto, P. R.; Padula, D.; Vilhena, J. G.; Prampolini, G. Accurate Quantum-Mechanically Derived Force-Fields through a Fragment-Based Approach: Balancing Specificity and Transferability in the Prediction of Self-Assembly in Soft Matter *J. Chem. Theory Comput.* **2022**, *18*, 6905–6919.

[108] De Mitri, N.; Monti, S.; Prampolini, G.; Barone, V. Absorption and Emission Spectra of a Flexible Dye in Solution: A Computational Time-Dependent Approach *J. Chem. Theory Comput.* **2013**, *9*, 4507–4516.

[109] Cerezo, J.; Santoro, F.; Prampolini, G. Comparing classical approaches with empirical or quantum-mechanically derived force fields for the simulation electronic lineshapes: application to coumarin dyes *Theor. Chem. Accounts* **2016**, *135*, 143.

[110] Andreussi, O.; Prandi, I. G.; Campetella, M.; Prampolini, G.; Mennucci, B. Classical Force Fields Tailored for QM Applications: Is It Really a Feasible Strategy? *J. Chem. Theory Comput.* **2017**, *13*, 4636–4648.

[111] Segalina, A.; Cerezo, J.; Prampolini, G.; Santoro, F.; Pastore, M. Accounting for Vibronic Features through a Mixed Quantum-Classical Scheme: Structure, Dynamics, and Absorption Spectra of a Perylene Diimide Dye in Solution *J. Chem. Theor. Comput.* **2020**, *16*, 7061–7077.

[112] Prampolini, G.; Yu, P.; Pizzanelli, S.; Cacelli, I.; Yang, F.; Zhao, J.; Wang, J. Structure and Dynamics of Ferrocyanide and Ferricyanide Anions in Water and Heavy Water: An Insight by MD Simulations and 2D IR Spectroscopy *J. Phys. Chem. B* **2014**, *118*, 14899–14912.

[113] Alborés, P.; Slep, L. D.; Weyhermüller, T.; Baraldo, L. M. Fine Tuning of the Electronic Coupling between Metal Centers in Cyano-Bridged Mixed-Valent Trinuclear Complexes *Inorganic Chemistry* **2004**, *43*, 6762–6773.

[114] Perdew, J. P.; Ernzerhof, M. Rationale for mixing exact exchange with density functional approximations *J. Chem. Phys.* **1996**, *105*, 9982–9985.

[115] Adamo, C.; Barone, V. Toward reliable density functional methods without adjustable parameters: The PBE0 model *J. Chem. Phys.* **1999**, *110*, 6158–6170.

[116] McLean, A. D.; Chandler, G. S. Contracted Gaussian basis sets for molecular calculations. I. Second row atoms, Z=11–18 *J. Chem. Phys.* **2008**, *72*, 5639–5648.

[117] Krishnan, R.; Binkley, J. S.; Seeger, R.; Pople, J. A. Self-consistent molecular orbital methods. XX. A basis set for correlated wave functions *J. Chem. Phys.* **2008**, *72*, 650–654.

[118] Dolg, M.; Wedig, U.; Stoll, H.; Preuss, H. Energy-adjusted ab initio pseudopotentials for the first row transition elements *J. Chem. Phys.* **1987**, *86*, 866–872.

[119] Andrae, D.; Häußermann, U.; Dolg, M.; Stoll, H.; Preuß, H. Energy-adjusted ab initio pseudopotentials for the second and third row transition elements *Theor. Chim. Acta* **1990**, *77*, 123–141.

[120] Liekhus-Schmaltz, C.; Fox, Z. W.; Andersen, A.; Kjaer, K. S.; Alonso-Mori, R.; Biasin, E.; Carlstad, J.; Chollet, M.; Gaynor, J. D.; Glownia, J. M.; Hong, K.; Kroll, T.; Lee, J. H.; Poulter, B. I.; Reinhard, M.; Sokaras, D.; Zhang, Y.; Doumy, G.; March, A. M.; Southworth, S. H.; Mukamel, S.; Cordones, A. A.; Schoenlein, R. W.; Govind,

N.; Khalil, M. Femtosecond X-ray Spectroscopy Directly Quantifies Transient Excited-State Mixed Valency *J. Phys. Chem. Lett.* **2022**, *13*, 378–386.

[121] Tomasi, J.; Mennucci, B.; Cammi, R. Quantum Mechanical Continuum Solvation Models *Chem. Rev.* **2005**, *105*, 2999–3094.

[122] Hirata, S.; Head-Gordon, M. Time-dependent density functional theory within the Tamm–Dancoff approximation *Chem. Phys. Lett.* **1999**, *314*, 291–299.

[123] Frisch, M. J.; Trucks, G. W.; Schlegel, H. B.; Scuseria, G. E.; Robb, M. A.; Cheeseman, J. R.; Scalmani, G.; Barone, V.; Petersson, G. A.; Nakatsuji, H.; Li, X.; Caricato, M.; Marenich, A. V.; Bloino, J.; Janesko, B. G.; Gomperts, R.; Mennucci, B.; Hratchian, H. P.; Ortiz, J. V.; Izmaylov, A. F.; Sonnenberg, J. L.; Williams-Young, D.; Ding, F.; Lipparini, F.; Egidi, F.; Goings, J.; Peng, B.; Petrone, A.; Henderson, T.; Ranasinghe, D.; Zakrzewski, V. G.; Gao, J.; Rega, N.; Zheng, G.; Liang, W.; Hada, M.; Ehara, M.; Toyota, K.; Fukuda, R.; Hasegawa, J.; Ishida, M.; Nakajima, T.; Honda, Y.; Kitao, O.; Nakai, H.; Vreven, T.; Throssell, K.; Montgomery, J. A., Jr.; Peralta, J. E.; Ogliaro, F.; Bearpark, M. J.; Heyd, J. J.; Brothers, E. N.; Kudin, K. N.; Staroverov, V. N.; Keith, T. A.; Kobayashi, R.; Normand, J.; Raghavachari, K.; Rendell, A. P.; Burant, J. C.; Iyengar, S. S.; Tomasi, J.; Cossi, M.; Millam, J. M.; Klene, M.; Adamo, C.; Cammi, R.; Ochterski, J. W.; Martin, R. L.; Morokuma, K.; Farkas, O.; Foresman, J. B.; Fox, D. J.; Gaussian˜16 Revision C.01; 2016; Gaussian Inc. Wallingford CT.

[124] Valiev, M.; Bylaska, E. J.; Govind, N.; Kowalski, K.; Straatsma, T. P.; Van Dam, H. J. J.; Wang, D.; Nieplocha, J.; Apra, E.; Windus, T. L.; de Jong, W. A. NWChem: A comprehensive and scalable open-source solution for large scale molecular simulations *Computer Physics Communications* **2010**, *181*, 1477–1489.

[125] Aprà, E.; Bylaska, E.; de Jong, W.; Govind, N.; Kowalski, K.; Straatsma, T.; Valiev, M.; van Dam, H.; Alexeev, Y.; Anchell, J.; Anisimov, V. ; Aquino, F. W. ; Atta-Fynn, R. ; Autschbach, J. ; Bauman, N. P. ; Becca, J. C. ; Bernholdt, D. E. ; Bhaskaran-Nair, K. ; Bogatko, S. ; Borowski, P. ; Boschen, J. ; Brabec, J. ; Bruner, A. ; Cauët, E. ; Chen, Y. ;

Chuev, G. N. ; Cramer, C. J. ; Daily, J. ; Deegan, M. J. O. ; Dunning, T. H., Jr. ; Dupuis, M. ; Dyall, K. G. ; Fann, G. I. ; Fischer, S. A. ; Fonari, A. ; Früchtl, H. ; Gagliardi, L. ; Garza, J. ; Gawe, N. ; Ghosh, S. ; Glaesemann, K. ; Götz, A.4W. ; Hammond, J. ; Helms, V. ; Hermes, E. D. ; Hirao, K. ; Hirata, S. ; Jacquelin, M. ; Jensen, L. ; Johnson, B. G. ; Jónsson, H. ; Kendall, R. A. ; Klemm, M. ; Kobayashi, R. ; Konkov, V. ; Krishnamoorthy, S. ; Krishnan, M. ; Lin, Z. ; Lins, R. D. ; Littlefield, R. J. ; Logsdail, A. J. ; Lopata, K. ; Ma, W. ; Marenich, A. V. ; Martin del Campo, J. ; Mejia-Rodriguez, D. ; Moore, J. E. ; Mullin, J. M. ; Nakajima, T. ; Nascimento, D. R. ; Nichols, J. A. ; Nichols, P. J. ; Nieplocha, J. ; Otero-de-la-Roza, A. ; Palmer, B. ; Panyala, A. ; Pirojsirikul, T. ; Peng, B. ; Peverati, R. ; Pittner, J. ; Pollack, L. ; Richard, R. M. ; Sadayappan, P. ; Schatz, G. C. ; Shelton, W. A. ; Silverstein, D. W. ; Smith, D. M.5A. ; Soares, T. A. ; Song, D. ; Swart, M. ; Taylor, H. L. ; Thomas, G. S. ; Tipparaju, V. ; Truhlar, D. G. ; Tsemekhman, K. ; Van Voorhis, T. ; Vázquez-Mayagoitia, Á. ; Verma, P. ; Villa, O. ; Vishnu, A. ; Vogiatzis, K. D. ; Wang, D. ; Weare, J. H. ; Williamson, M. J. ; Windus, T. L. ; Woliński, K. ; Wong, A. T. ; Wu, Q. ; Yang, C. ; Yu, Q. ; Zacharias, M. ; Zhang, Z. ; Zhao, Y. ; Harrison, R. J. NWChem: Past, present, and future *J. Chem. Phys.* **2020**, *152*, 184102.

[126] Wang, J.; Wolf, R. M.; Caldwell, J. W.; Kollman, P. a.; Case, D. a. Development and Testing of a General Amber Force Field. *J. Comp. Chem.* **2004**, *25*, 1157–74.

[127] Cygan, R. T.; Liang, J.-J.; Kalinichev, A. G. Molecular Models of Hydroxide, Oxyhydroxide, and Clay Phases and the Development of a General Force Field *J. Phys. Chem. B* **2004**, *108*, 1255–1266.

[128] Berendsen, H. J. C.; Grigera, J. R.; Straatsma, T. P. The missing term in effective pair potentials *J. Phys. Chem.* **1987**, *91*, 6269–6271.

[129] Joung, I. S.; Cheatham, T. E. Determination of Alkali and Halide Monovalent Ion Parameters for Use in Explicitly Solvated Biomolecular Simulations *J. Phys. Chem. B* **2008**, *112*, 9020–9041.

[130] Ryckaert, J.-P.; Ciccotti, G.; Berendsen, H. J. C. Numerical integration of the cartesian equations of motion of a system with constraints: molecular dynamics of n-alkanes *J. Comp. Phys.* **1977**, *23*, 327–341.

[131] Berendsen, H. J. C.; Postma, J. P. M.; van Gunsteren, W. F.; DiNola, A.; Haak, J. R. Molecular dynamics with coupling to an external bath *J. Chem. Phys.* **1984**, *81*, 3684–3690.

[132] Cacelli, I.; Cerezo, J.; ; De Mitri, N.; Prampolini, G.; JOYCE2.10, a Fortran 77 code for intra-molecular force field parameterization. , available free of charge at http://www.iccom.cnr.it/en/joyce-2, last consulted Septemb er 2022; 2013.

[133] Barone, V.; Cacelli, I.; De Mitri, N.; Licari, D.; Monti, S.; Prampolini, G. Joyce and Ulysses: Integrated and User-Friendly Tools for the Parameterization of Intramolecular Force Fields from Quantum Mechanical Data. *Phys. Chem. Chem. Phys.* **2013**, *15*, 3736–51.

[134] Cerezo, J.; Prampolini, G.; Cacelli, I. Developing accurate intramolecular force fields for conjugated systems through explicit coupling terms *Theor. Chem. Accounts* **2018**, *137*, 80.

[135] Adlhart, C.; Chen, P. Ligand Rotation Distinguishes First- and Second-Generation Ruthenium Metathesis Catalysts *Angew. Chem. Int. Ed.* **2002**, *41*, 4484–4487.

[136] Aguilar, C. M.; De Almeida, W. B.; Rocha, W. R. The electronic spectrum of Fe2+ ion in aqueous solution: A sequential Monte Carlo/quantum mechanical study *Chem. Phys. Lett.* **2007**, *449*, 144–148.

[137] Jorgensen, W. L.; Chandrasekhar, J.; Madura, J. D.; Impey, R. W.; Klein, M. L. Comparison of simple potential functions for simulating liquid water *J. Chem. Phys.* **1983**, *79*, 926–935.

[138] Marenich, A. V.; Jerome, S. V.; Cramer, C. J.; Truhlar, D. G. Charge Model 5: An Extension of Hirshfeld Population Analysis for the Accurate Description of Molecular

Interactions in Gaseous and Condensed Phases *J. Chem. Theory Comput.* **2012**, *8*, 527–541.

[139] Bussi, G.; Donadio, D.; Parrinello, M. Canonical sampling through velocity rescaling *J. Chem. Phys.* **2007**, *126*, 014101.

[140] Parrinello, M.; Rahman, A. Polymorphic transitions in single crystals: A new molecular dynamics method *J. Appl. Phys.* **1981**, *52*, 7182–7190.

[141] Iftimie, R.; Tuckerman, M. E. Decomposing total IR spectra of aqueous systems into solute and solvent contributions: A computational approach using maximally localized Wannier orbitals *J. Chem. Phys.* **2005**, *122*, 214508.

[142] Gaigeot, M.-P.; Sprik, M. Ab Initio Molecular Dynamics Computation of the Infrared Spectrum of Aqueous Uracil *J. Phys. Chem. B* **2003**, *107*, 10344–10358.

[143] Coe, B. J. Syntheses and Characterization of Ruthenium(II) Tetrakis(Pyridine) Complexes. An Advanced Coordination Chemistry Experiment or Mini-Project *J. Chem. Ed.* **2004**, *81*, 718.

[144] Pawlak, R.; Vilhena, J. G.; D'Astolfo, P.; Liu, X.; Prampolini, G.; Meier, T.; Glatzel, T.; Lemkul, J. A.; Häner, R.; Decurtins, S.; Baratoff, A.; Pérez, R.; Liu, S.-X.; Meyer, E. Sequential Bending and Twisting around C–C Single Bonds by Mechanical Lifting of a Pre-Adsorbed Polymer *Nano Lett.* **2020**, *20*, 652–657.

[145] Vilhena, J. G.; Pawlak, R.; D'Astolfo, P.; Liu, X.; Gnecco, E.; Kisiel, M.; Glatzel, T.; Pérez, R.; Häner, R.; Decurtins, S.; Baratoff, A.; Prampolini, G.; Liu, S.-X.; Meyer, E. Flexible Superlubricity Unveiled in Sidewinding Motion of Individual Polymeric Chains *Phys. Rev. Lett.* **2022**, *128*, 216102.

[146] Alecu, I. M.; Zheng, J.; Zhao, Y.; Truhlar, D. G. Computational Thermochemistry: Scale Factor Databases and Scale Factors for Vibrational Frequencies Obtained from Electronic Model Chemistries *J. Chem. Theory Comput.* **2010**, *6*, 2872–2887.

[147] Slenkamp, K. M.; Lynch, M. S.; Van Kuiken, B. E.; Brookes, J. F.; Bannan, C. C.; Daifuku, S. L.; Khalil, M. Investigating vibrational anharmonic couplings in cyanide-bridged transition metal mixed valence complexes using two-dimensional infrared spectroscopy *J. Chem. Phys.* **2014**, *140*, 084505.

[148] Cerezo, J.; Aranda, D.; Avila Ferrer, F. J.; Prampolini, G.; Santoro, F. Adiabatic-Molecular Dynamics Generalized Vertical Hessian Approach: A Mixed Quantum Classical Method to Compute Electronic Spectra of Flexible Molecules in the Condensed Phase *J. Chem. Theory Comput.* **2020**, *16*, 1215–1231.

[149] Ronca, E.; Pastore, M.; Belpassi, L.; De Angelis, F.; Angeli, C.; Cimiraglia, R.; Tarantelli, F. Charge-displacement analysis for excited states *J. Chem. Phys.* **2014**, *140*.

[150] Ronca, E.; Angeli, C.; Belpassi, L.; De Angelis, F.; Tarantelli, F.; Pastore, M. Density relaxation in time-dependent density functional theory: Combining relaxed density natural orbitals and multireference perturbation theories for an improved description of excited states *J. Chem. Theor. Comput.* **2014**, *10*, 4014–4024.

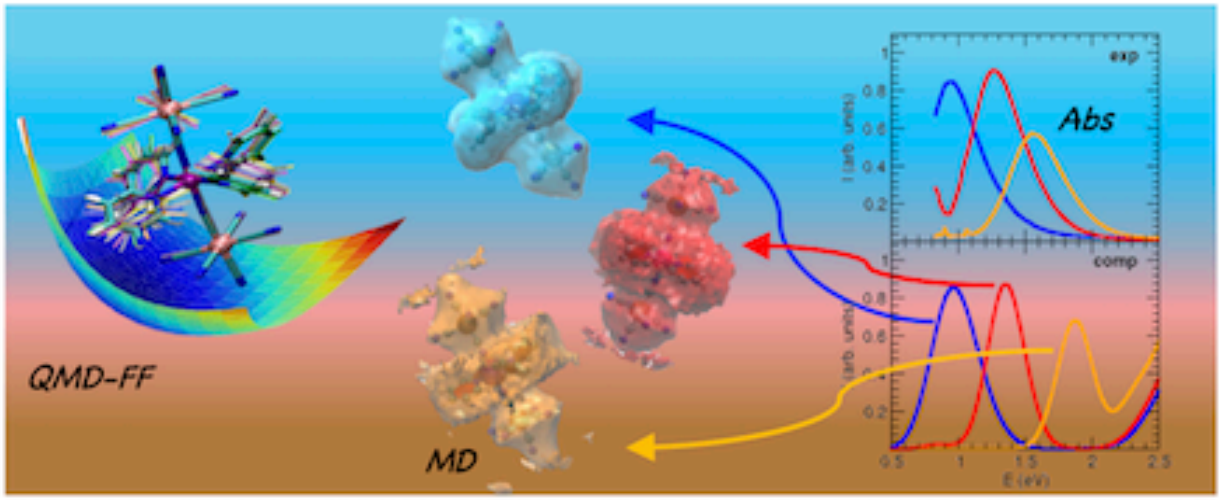

TOC: Accurate force-fields, tailored against the quantum mechanical potential energy surface of the complex, are employed in classical molecular dynamics to unravel the observed solvatochromic properties..